sustainability

MDPI

Article

Fully Coupled Analysis of a 10 MW Floating Wind Turbine Integrated with Multiple Wave Energy Converters for Joint Wind and Wave Utilization

Wei Jiang [1], Chenyu Liang [2,3], Tao Tao [4], Yi Yang [4], Shi Liu [4], Jiang Deng [2] and Mingsheng Chen [2,3,*]

[1] China Datang Corporation, Ltd., Guangdong Branch, Guangzhou 510000, China; jiangwei_cdt@126.com
[2] School of Naval Architecture, Ocean and Energy Power Engineering, Wuhan University of Technology, Wuhan 430063, China; 348349@whut.edu.cn (C.L.); 272022@whut.edu.cn (J.D.)
[3] Sanya Science and Education Innovation Park, Wuhan University of Technology, Sanya 572019, China
[4] China Southern Power Grid Technology Co., Ltd., Guangzhou 510080, China; taot0804@163.com (T.T.); yyxt007@sina.cn (Y.Y.); 13925041516@139.com (S.L.)
* Correspondence: mschen@whut.edu.cn; Tel.: +86-182-7193-5791

Abstract: The study focuses on a semi-submersible wind-wave integrated power-generation platform, which consists of an OO-Star semi-submersible platform equipped with a DTU 10 MW wind turbine and a set of wave energy converters. A hydrodynamic model was established using ANSYS-AQWA (2023 R1), and by incorporating upper wind loads and utilizing the open-source program F2A, a fully coupled time-domain model of the integrated power-generation platform was constructed. The primary objective is to explore the interaction mechanisms between the upper wind turbine and the lower wave energy devices under the combined effects of irregular waves and turbulent wind through a series of operational conditions. Additionally, the safety of the mooring system was assessed. The results indicate that, compared to the wave period, the power generation of the lower wave energy devices is more significantly affected by wave height. Overall, the integrated power-generation platform demonstrates optimal performance under the third operational condition. In survival conditions, the introduction of oscillating buoys can improve the motion responses of the platform in terms of sway, roll, pitch, and yaw to a certain extent, but it also increases the surge and heave motion responses and the associated mooring loads. The mooring system can ensure the safety of the integrated power-generation platform under extreme sea conditions.

Keywords: semi-submersible platform; wind-wave integrated power generation; mooring system; wave energy converters

check for updates

Citation: Jiang, W.; Liang, C.; Tao, T.; Yang, Y.; Liu, S.; Deng, J.; Chen, M. Fully Coupled Analysis of a 10 MW Floating Wind Turbine Integrated with Multiple Wave Energy Converters for Joint Wind and Wave Utilization. *Sustainability* **2024**, *16*, 9172. https://doi.org/10.3390/su16219172

Received: 12 September 2024
Revised: 18 October 2024
Accepted: 20 October 2024
Published: 22 October 2024

Copyright: © 2024 by the authors. Licensee MDPI, Basel, Switzerland. This article is an open access article distributed under the terms and conditions of the Creative Commons Attribution (CC BY) license (https://creativecommons.org/licenses/by/4.0/).

1. Introduction

Renewable energy, as a crucial strategy for addressing global energy and environmental challenges, is receiving increasing attention. Offshore wind power, as a significant component of renewable energy, has shown a strong growth trend. According to the *GLOBAL WIND REPORT 2023* [1] released by the Global Wind Energy Council (GWEC), offshore wind power has made remarkable progress worldwide over the past decade, with total installed capacity steadily increasing year by year, technological advancements continuously improving, and costs steadily decreasing. However, floating power platforms that rely solely on wind energy have certain limitations in terms of resource utilization and energy stability.

Many scholars have proposed the concept of hybrid power-generation platforms that combine wind energy and wave energy, based on the comprehensive utilization of marine energy. These floating wind-wave hybrid power platforms can optimize the allocation of energy resources and leverage the complementary nature of the two energy sources, overcoming the limitations of relying solely on wind energy for power generation.

Although wave energy has a relatively lower energy density, it offers greater stability and continuity. By integrating wave energy generation devices into floating wind turbines, the intermittency of wind energy can be compensated, enabling the synergistic use of both energy sources, thus enhancing the stability and reliability of the power-generation system.

The floating wind-wave hybrid power platform is based on a floating wind turbine and is subjected to complex loads such as wind, waves, and currents. When combined with wave energy generation devices, it is necessary to consider the interaction between these devices and the floating wind turbine, making the motion response and power-generation mechanisms of the hybrid system relatively complex. In recent years, with the in-depth exploration of the conceptual design of wind-wave hybrid power-generation devices, many scholars have employed numerical simulation methods to integrate floating wind turbines with wave energy generation devices, achieving fully coupled aero-hydro-servo-elastic dynamic analysis. Overall, numerical simulation methods can be categorized into three types. The first type involves adding a hydrodynamic analysis module to numerical analysis programs originally designed for wind turbines, such as FAST and HAWC2. The second type couples an aerodynamic module with a hydrodynamic analysis program, such as SIMO-RIFLEX-AeroDyn [2] and F2A [3,4]. Additionally, some independently developed programs, such as Aquaplus [5], which is based on the Boundary Element Method (BEM), can be used to calculate the hydrodynamic coefficients of wind-wave hybrid platforms like "C-HyP".

Zhou et al. [6] from Dalian University of Technology, along with Cong et al. [7], utilized a three-dimensional time-domain numerical model based on a higher-order boundary element method to study the coupled hydrodynamic response of a cylindrical OWC (Oscillating Water Column) device, with a focus on the dynamic coupling between floating wind turbines and WECs (Wave Energy Converters). Jang et al. [8] employed a self-developed program called "Multi-Unit Floating Offshore Wind Turbine" (MUFOWT) to simulate a system combining multiple wind turbines with WECs. This system allows for the extension and modification of programs such as FAST and CHARM3D, enabling the two programs to exchange data at each time step. Yang developed a co-simulation method called F2A for FAST/AQWA, which compiles the open-source program FAST, integrating aerodynamic, structural dynamic, and servo systems, into a dynamic link library. This library is then called by AQWA's User-force function to establish an aero-hydro-servo-elastic coupled analysis model. Li et al. [9] used two numerical simulation methods to simulate the motion response and power characteristics of a hybrid power-generation platform. One method is based on the coupled open-source code F2A, which integrates the FAST and AQWA tools to account for all possible environmental loads; the other method uses only AQWA. The results of these two methods show significant differences in the time-domain motion response and mooring performance under irregular waves and turbulent wind conditions, demonstrating the importance of considering aerodynamic damping effects in hybrid power-generation systems. Cheng et al. [10] conducted a numerical analysis of a hybrid power-generation platform using the SIMO-RIFLEX-DMS approach. Peiffer et al. [11] analyzed the dynamic response of a hybrid power-generation platform through coupled analysis using OrcaFlex 11.4b and WAMIT 7.0. Ren et al. [12] utilized AQWA and AeroDyn to perform numerical simulations of a monopile offshore wind turbine combined with a heave-type WEC (Wave Energy Converter). The hydrodynamic characteristics of the WEC and the maximum PTO damping force obtained from the study provide valuable guidance for the optimal design of the PTO system's operational performance. Li et al. [13] used a combination of WindSloke and WEC-Sim for coupled simulations, showing that real-time data interaction between simulation modules is crucial. Si et al. [14] applied the F2A method to their newly designed wind-wave combined power-generation platform, conducting a couple dynamic response study of wind and wave and optimizing the control strategy of the wave energy conversion device on the platform. Wang et al. [15] developed a simulation model of the wind-wave combined power-generation platform using AMESim and MATLAB/Simulink. They compared the output power, generator speed,

system pressure, and internal flow of the combined power-generation system with two independent power-generation systems, evaluating the performance of complementary power generation. Wang et al. [16] focused on a floating combined power-generation system, where they mathematically modeled the WEC hydraulic PTO system using hydraulic component equations, established a MATLAB/Simulink-based simulation framework, and validated it. They investigated the impact of six key hydrodynamic parameters on the energy capture and motion response performance of the combined power-generation system under a wide range of wave conditions. However, these studies did not address the interaction mechanisms between multiple wave energy conversion devices and the interactions between wave energy devices and wind turbines.

Therefore, considering the coupling effects among the aerodynamic loads of the wind turbine, wave loads on the floating wind power platform, and flow loads on the arrayed wave energy converters, a fully coupled time-domain model of the floating wind-wave integrated power-generation platform was established in AQWA. This model integrates aerodynamic, structural dynamic, servo control, hydrodynamic, and mooring systems. Using CATIFES, the dynamic responses of the semi-submersible wind-wave integrated power-generation platform, which consists of the OO-Star semi-submersible platform, the DTU 10 MW wind turbine, and wave energy converters under different array configurations, were calculated under the combined effects of wind, wave, and current loads. The study quantitatively analyzed the impact of the upper wind turbine and wave energy converters on platform motion responses, mooring tension, and system output power, providing a reference for the design of floating multi-energy integrated system.

2. Materials and Methods

2.1. Mooring Theory

When calculating mooring loads, the lumped mass method is typically used to discretize the dynamics of the mooring lines. As shown in Figure 1, a mooring line is divided into N uniform segments, connecting N + 1 nodes. The mooring line starts from the anchor point (or lower end), with the value of the anchor node being 0. The segment of the mooring line between node 0 and node 1 is indexed as 1/2. This model uses a right-handed inertial reference frame, with the z-axis origin located at the horizontal plane, and the position of each node is defined by the vector r. Each segment of the mooring line has the same unstretched length, diameter, density, and Young's modulus. Different mooring lines can have different characteristics, and the lines can be connected at both ends, allowing the mooring system to form interconnected lines.

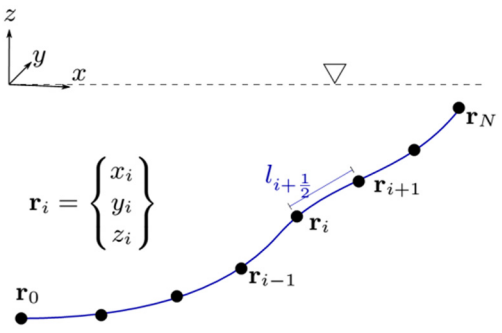


Figure 1. Schematic diagram of concentrated mass method.

Based on the above method, for a single-component mooring line in a catenary state without considering the elasticity of the line, the lowest point is tangent to the seabed, with a corresponding inclination angle of zero. At this point, the mooring tension T is equal to

the horizontal component of the tension at any point along the suspended part of the line. The corresponding key formulas are as follows [17]:

$$l_0 = asinh\left(\frac{S}{a}\right) \tag{1}$$

$$H = a[cosh(S/a) - 1] \tag{2}$$

$$l_0 = \sqrt{H^2 + 2Ha} \tag{3}$$

$$a = T_H/w \tag{4}$$

The maximum tension at the top end of the mooring line can be expressed as [18]:

$$T_{\max} = T_H + wH \tag{5}$$

where: w represents the submerged weight of the mooring line per unit length; H represents the water depth; l is the total length of the mooring line; T is the horizontal tension at the point of contact with the seabed; S is the horizontal distance between the point of maximum tension at the top end and the seabed contact point; l_0 represents the length of the suspended section of the mooring line, as shown in Figure 2.

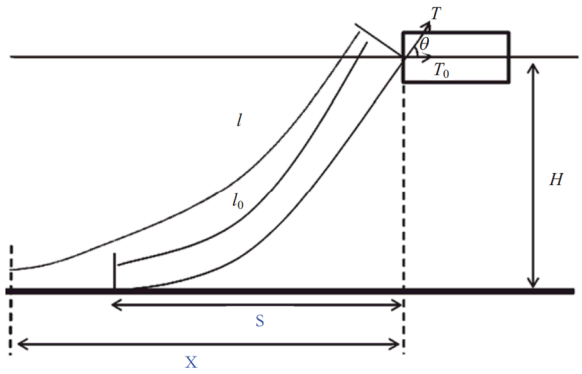


Figure 2. Schematic diagram of parameters of catenary equations.

When the water depth H, the weight w of the cable per unit length in water, and the horizontal tension T_0 are known, the cable length l_0 corresponding to the tangent position of the lower end of the cable, the tension T at the top of the mooring cable and its inclination, and the horizontal span S between the top and the tangent position of the seabed can be solved.

When the water depth H, the length of the mooring cable l, and the weight per unit length in water w are known, the maximum horizontal tension $T_{\max}$ that can be sustained by the lower end in the horizontal direction can be solved. At this time, a judgment needs to be made: if $T_0 < T_{\max}$, the mooring cable has a horizontal chain length, based on which other parameters can be calculated; if $T_0 > T_{\max}$, the mooring cable is fully pulled up, and the anchor point will be affected by the upward pull force.

However, the mooring cable is elastic, and the conclusion obtained by ignoring the elastic effect of the mooring cable in some scenarios is inaccurate. The length l_0 of the mooring cable suspension section that has not been stretched can be expressed as:

$$l_0 = \frac{T_z}{w} \tag{6}$$

where T_z is the vertical force on the upper mooring point, which is equal to the vertical weight of the mooring cable hanging in the water.

$$H = T_0/w\left[\frac{1}{cos\phi_w} - 1\right] + \frac{1}{2}\frac{w}{AE}{l_0}^2 \tag{7}$$

$$cos\theta = \frac{T_H}{\sqrt{{T_H}^2 + {T_Z}^2}} \tag{8}$$

where A represents the cross-sectional area of the mooring line, E represents the elastic modulus of the mooring material, θ is the angle between the axial tension at the mooring point and the horizontal force T_0:

$$T_0 = \frac{T_Z^2 - \left(wH - \frac{1}{2}\frac{w^2}{AE}{l_0}^2\right)^2}{2\left(wH - \frac{1}{2}\frac{w^2}{AE}{l_0}^2\right)} \tag{9}$$

The tension at the top of the mooring line can be expressed as:

$$T = \sqrt{{T_H}^2 + {T_Z}^2} \tag{10}$$

$$S = \frac{T_H}{w}log(\frac{\sqrt{{T_H}^2 + {T_Z}^2} + T_Z}{T_H}\Bigg) + \frac{T_H}{AE}l_0 \tag{11}$$

In specific calculations, we can first assume a T_Z, and then calculate l_0, T_0, T, and S according to Equations (6) and (9)–(11). When T_0 is known, calculate each T_Z according to the above steps, and then interpolate according to the data to finally obtain a suitable solution.

2.2. Wave Theory

In real sea conditions, waves are generally irregular and random. Irregular waves can be regarded as the linear superposition of regular waves with different parameters. Therefore, unlike wave height and period, which are precisely described in regular wave theory, in engineering practice, significant wave height and peak period are typically used to describe the characteristics of irregular waves.

Currently, the commonly used wave spectra include the Pierson–Moskowitz (P-M) spectrum, Bretschneider spectrum, ITTC spectrum, and the Joint North Sea Wave Project (JONSWAP) spectrum. Additionally, wave spectra can be established based on the measured wave characteristics specific to local sea conditions. This paper primarily utilizes the JONSWAP spectrum to analyze the motion response of floating bodies under irregular waves, with its specific expression as follows [19]:

$$S(\omega) = \frac{5}{16} \cdot H_s^2\omega_p^4 \cdot \omega^{-5}exp\left(-\frac{5\omega_p^4}{4\omega^4}\right) \cdot A_\gamma \cdot \gamma^a \tag{12}$$

where H_s represents the significant wave height, ω_p is the peak frequency, γ is the peak enhancement factor, and $A_\gamma = 1 - 0.287\ln(\gamma)$ is the normalization constant. Additionally, the coefficient can be expressed as [20]:

$$a = exp[-\frac{(\omega - \omega_p)^2}{2\sigma^2\omega_p^2}] \tag{13}$$

When $\omega \leq \omega_p$, $\sigma = 0.07$; when $\omega > \omega_p$, $\sigma = 0.09$.

2.3. Time Domain Motion Equation

For the floating wind-wave combined platform, based on the multi-body frequency-domain constraint model [21], a three -degree -of -freedom time-domain motion model of the wind-wave combined power-generation platform is established, simultaneously considering the constraints of the PTO (Power Take-Off) system and the end-stop system. This model is based on the Cummins equation, which describes the interaction between the floating body and the waves [22]:

$$[\mathbf{M} + \mathbf{A}(\infty)]\ddot{\mathbf{x}}(t) + \int_0^t \mathbf{K}(t-\tau)\dot{\mathbf{x}}(\tau)d\tau + \mathbf{C}\mathbf{x}(t) = \mathbf{F}^{exc}(t) + \mathbf{F}^{est}(t) \tag{14}$$

where $\mathbf{A}(\infty)$ denotes the infinite-frequency added mass matrix of the catamaran float-over system; $\mathbf{K}(t)$ refers to the matrix of the retardation function, which is the kernel of the convolution term representing the fluid memory effects; $\mathbf{x}(t)$ is the vector of time-domain responses; $\mathbf{F}^{exc}(t)$ denotes the vector of time-domain wave excitation forces, $\mathbf{F}^{est}(t)$ denotes the constraint force in the end-stop system.

$$\mathbf{x}(t) = \begin{bmatrix} x_3(\omega t) \\ x_4(\omega t) \\ x_5(\omega t) \\ x_9(\omega t) \end{bmatrix} \tag{15}$$

where **x** is the displacement of the floating body, subscripts 3, 4, and 5 represent the degrees of freedom in the heave, roll, and pitch directions of the floating platform, and subscript 9 represents the degree of freedom in the heave direction of the oscillating float.

The following transformation relationship exists between the radiation damping coefficient and the impulse response function:

$$\mathbf{K}(t) = \frac{2}{\pi}\int_0^\infty \mathbf{B}(\omega)cos(\omega t)d\omega \tag{16}$$

Therefore, based on the added mass $\mathbf{A}(\omega)$ and radiation damping of the floating body $\mathbf{B}(\omega)$, the added mass of the floating body at infinite frequency can be derived according to Equation (14):

$$\mathbf{A}(\infty) = \frac{1}{N}\sum_{n=1}^{N}\left(\mathbf{A}(\omega_n) + \frac{1}{\omega_n}\int_0^\infty \mathbf{K}(t)sin\omega_n t dt\right) \tag{17}$$

The load of the end-stop system can be obtained through the relative heave motion between the oscillating buoy and the floating foundation. If the end-stop system essentially behaves as a linear spring, the load exerted on the floating foundation can be expressed as [23]:

$$F_3^{est} = \begin{cases} -k(x_3 - x_9 - e) & x_3 - x_9 > e or x_3 - x_9 < -e \\ 0 & -e \le x_3 - x_9 \le e \end{cases} \tag{18}$$

where k represents the stiffness of the upper and lower springs in the end-stop system; e represents the gap between the oscillating buoy and the end-stop spring.

The convolution term in the above model represents the influence of wave radiation force on the floating body. Directly solving this term requires a long simulation time and results in low computational efficiency. Therefore, based on Zou's method [24], this paper uses a state-space model to replace the computationally intensive convolution term.

$$\begin{aligned} \dot{\boldsymbol{z}}(t) &= \boldsymbol{A}\cdot z(t) + \boldsymbol{B}\cdot\dot{x}(t) \\ y\left(\dot{x}(t)\right) &= \boldsymbol{C}\cdot\boldsymbol{z}(t) \end{aligned} \tag{19}$$

where $A \in R^{n\times n}$, $B \in R^{n\times 1}$, and $C \in R^{1\times n}$ are constant coefficient matrices constructed based on the state-space model, n is the order of the state-space, $z(t) \in R^{n\times 1}$ is the state

vector representing the time-accumulated effects, $y(\dot{x}(t))$ is the motion response output from the state-space.

Based on the time domain model constructed by Equation (14), the mooring load at the bottom of the platform is further introduced, and the combined effects of the aerodynamic, elastic, and servo loads of the upper wind turbine are considered. The six degrees of freedom fully coupled model of the floating wind-wave combined power-generation platform is as follows:

$$\begin{aligned}[\mathbf{M}+\mathbf{A}(\infty)]\begin{bmatrix}\ddot{\boldsymbol{X}}_P(t)\\ \ddot{\boldsymbol{X}}_F(t)\end{bmatrix}+\int_0^t[\mathbf{K}(t-\tau)+\boldsymbol{B}_v]\begin{bmatrix}\dot{\boldsymbol{X}}_P(\tau)\\ \dot{\boldsymbol{X}}_F(\tau)\end{bmatrix}d\tau+\mathbf{C}\begin{bmatrix}\boldsymbol{X}_P(\tau)\\ \boldsymbol{X}_F(\tau)\end{bmatrix}\\ =\begin{bmatrix}\boldsymbol{F}_P^{EXC}(t)\\ \boldsymbol{F}_F^{EXC}(t)\end{bmatrix}+\begin{bmatrix}\boldsymbol{F}_P^{PTO}(t)\\ \boldsymbol{F}_F^{PTO}(t)\end{bmatrix}+\begin{bmatrix}\boldsymbol{F}_P^{ESP}(t)\\ \boldsymbol{F}_F^{ESP}(t)\end{bmatrix}+\begin{bmatrix}\boldsymbol{F}_P^{M}(t)\\ 0\end{bmatrix}+\begin{bmatrix}\boldsymbol{F}_P^{W}\\ 0\end{bmatrix}\end{aligned} \tag{20}$$

where the subscripts F and P represent the oscillating buoy and semi-submersible foundation, respectively. $\mathbf{K}(t)$ refers to the matrix of the retardation function, $\boldsymbol{B}_v$ refers to viscous damping matrix, $\mathbf{C}$ represents the hydrostatic stiffness matrix, $\mathbf{F}^{EXC}(t)$ refers to the wave excitation force matrix, $\mathbf{F}^{PTO}(t)$ refers to the load matrix due to the PTO system, $\mathbf{F}^{ESP}(t)$ refers to the load matrix due to the end stop system. Both forces can be modeled numerically using the Fender module in ANSYS-AQWA; $\mathbf{F}^{M}(t)$ refers to the mooring loads for floating platforms, $\mathbf{F}^{W}(t)$ refers to the aerodynamic load of the upper wind turbine. This section is based on the open-source program F2A, which is called OPENFAST-3.0.0 for coupled calculations.

If the wave energy generation power in the time domain is specified to be related only to the heave motion, the instantaneous power generation of the Nth buoy can be expressed as [25]:

$$P_{ins(N)}=B_{pto}^{N}\left(\dot{x}_3(t)-\dot{x}_{(6N+3)}(t)\right)^2 \tag{21}$$

where B_{pto}^{N} represents the PTO damping of the Nth buoy, $x_3(t)$ and $x_{(6N+3)}(t)$ represent the heave motions of the floating platform and the oscillating buoy, respectively. Based on the instantaneous power generation, the average power generation for each buoy can be obtained as [26,27]:

$$P_{ave(N)}=\frac{1}{t_p}\int_0^{t_p}B_{pto}^{N}\left(\dot{x}_3{}^2(t)-\dot{x}_{(6N+3)}{}^2(t)\right)d\tau \tag{22}$$

where t_P represents the operation time.

3. Wind and Wave Combined Power-Generation Platform System Model

3.1. Semi-Submersible Platform and Mooring Design Parameters

The wind-wave integrated power-generation platform primarily relies on the relative heave motion between the oscillating floaters and the floating foundation to generate electricity. To study this coupled motion, this paper first conducted geometric modeling of the floating foundation and the oscillating floaters. The floating foundation is the OO-Star three-column semi-submersible foundation from the EU LIFE50+ project, which supports a DTU 10 MW wind turbine [28]. As shown in Figure 3, the platform is equipped with four columns. This foundation is suitable for a water depth of 130 m, with the wind turbine installed on the central column. Additionally, a 0.5-m-thick heave plate is installed at the bottom to improve its vertical motion response.

The floating foundation is 31.5 m high with a draft of 22 m. Its main parameters are shown in Table 1.

The mooring system adopts the official mooring scheme of the OO-Star, which uses three mooring lines of equal length, arranged uniformly with a 120° angle between them, attached to the outer sides of the tops of the three columns. Additionally, each mooring line

is equipped with 50,000 kg in the middle section to enhance mooring stability. The specific parameters of the mooring system are shown in Table 2.

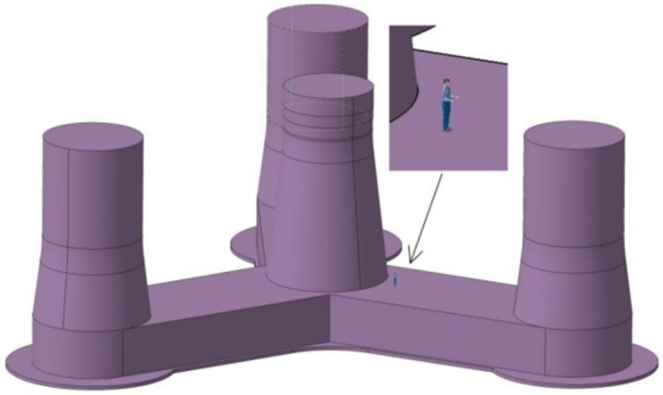


Figure 3. OO-Star three-column semi-submersible floating foundation.

Table 1. OO-Star semi-submersible floating foundation parameters.

Parameter	Value
Total mass (kg)	2.1709×10^7
Vertical center of gravity depth (m)	15.225
Vertical center of buoyancy depth (m)	14.236
Draft (m)	22
Displacement (m^3)	2.3509×10^7
Ixx ($kg \cdot m^2$)	9.43×10^6
Iyy ($kg \cdot m^2$)	9.43×10^6
Izz ($kg \cdot m^2$)	1.63×10^6

Table 2. Parameters of the mooring system.

Parameter	Value
Number of Mooring Lines	3
Mooring Line Dry Weight/(kg/m)	375.38
Wet Weight/kg	50,000
Unstretched Length of Mooring Line, Upper Segment/m	118
Unstretched Length of Mooring Line, Lower Segment/m	585
Mooring Radius/m	691
Mooring Line Stiffness/N	1.506×10^9
Fairlead Radius/m	44
Fairlead Height Above Water Surface/m	9.5

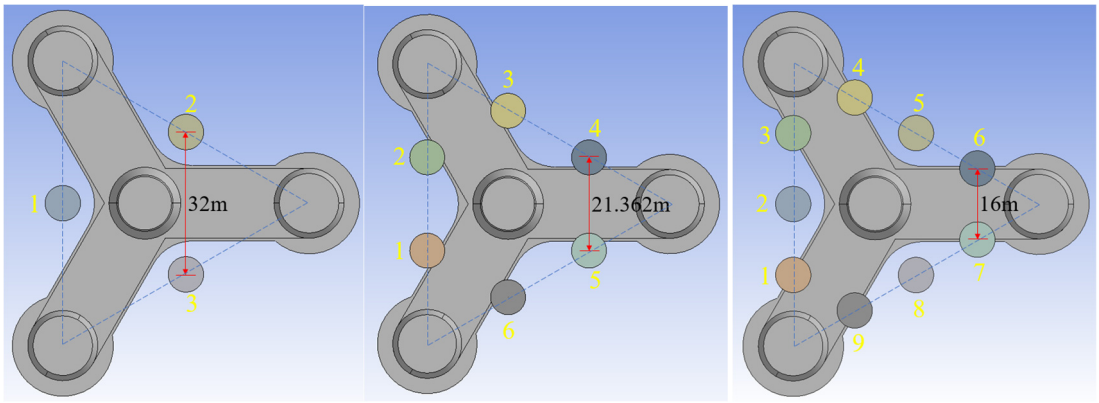
3.2. Wind Turbine and Array Float Design Model

The wind turbine selected is a 10 MW three-blade horizontal-axis wind turbine designed by the Technical University of Denmark (DTU). The main design parameters of the wind turbine are shown in Table 3.

Subsequently, an array of oscillating floaters was introduced. In this study, the oscillating floater is simplified as a cylindrical structure connected to a PTO device [29] at the top and bottom. The cylinder has a radius of 4 m, a height of 5 m, and a draft of 3 m. To achieve an array arrangement of the floaters on the three crossbeams of the floating foundation, three types of arrays were configured with the floater center spacing as a variable, and the floaters were numbered as shown in Figure 4. The spacings between floaters in the three array configurations are 32 m, 21.362 m, and 16 m, respectively.

Table 3. Main design parameters of the DTU 10 MW wind turbine.

Parameter	Value
Frequency/MW	10
Number of Blades	3
Rotor Diameter/m	178.3
Hub Diameter/m	5.6
Hub Height/m	119
Maximum Tip Speed/(m/s)	90.0
Cut-in Wind Speed/(m/s)	4.0
Cut-outWind Speed/(m/s)	25.0
Rated Wind Speed/(m/s)	11.4
Rotor Mass/kg	2.27962×10^5
Tower Mass/kg	1.25700×10^6
Nacelle Mass/kg	4.46036×10^5



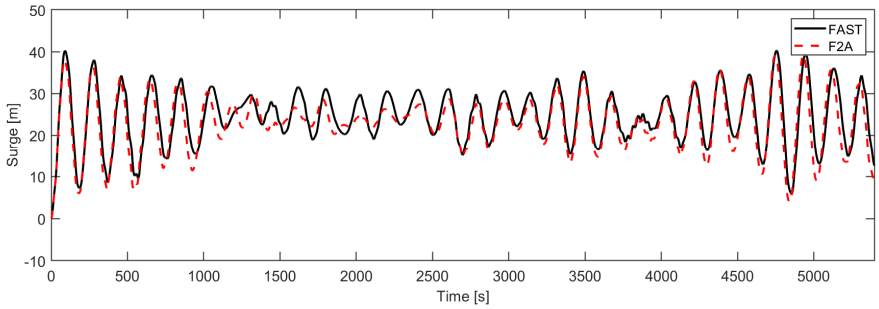
(**a**) Three-floater array. (**b**) Six-floater array. (**c**) Nine-floater array.

Figure 4. Schematic diagram of three types of oscillating floater array arrangements.

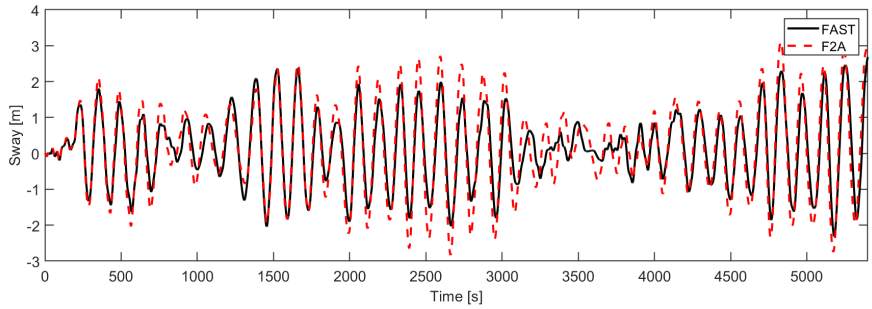
4. Result

4.1. Fully Coupled Model Construction and Verification

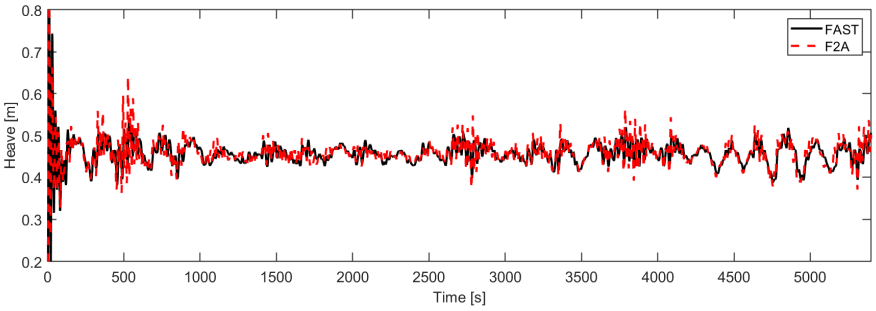
Before constructing the fully coupled analysis model for the wind-wave combined power-generation platform, it is necessary to first validate the F2A method. This paper compares the results of OPENFAST-3.0.0 with those of F2A, selecting the motion response of a single platform for validation. Both methods use turbulent wind at the wind turbine's rated wind speed of 11.4 m/s for verification, with the turbulent wind generated by the IECKAI turbulence model at the reference height of the turbine hub. The wave conditions are set as still water to eliminate the interference of wave seed randomness on the results. As shown in Figure 5, the time-domain comparison of the six degrees of freedom platform responses from both methods indicates good overall agreement, except for the surge and roll amplitudes where the F2A results show slightly larger amplitudes compared to FAST. This difference is primarily because the hydrodynamic coefficients in FAST are derived based on a center of gravity height of zero, which results in reduced stability compared to the original model, leading to greater motion amplitudes. Overall, the F2A method demonstrates high accuracy and is suitable for subsequent coupled motion analysis.



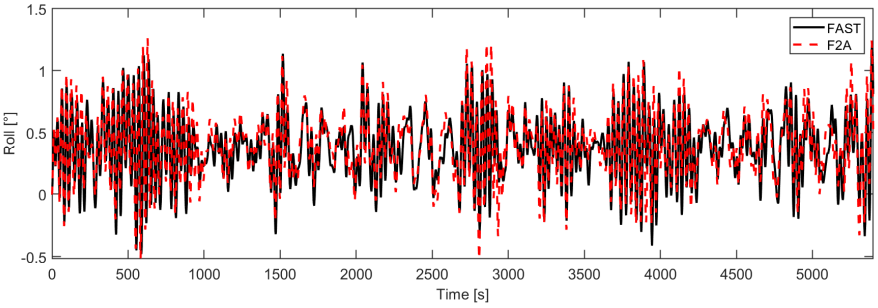
(**a**) Platform Surge



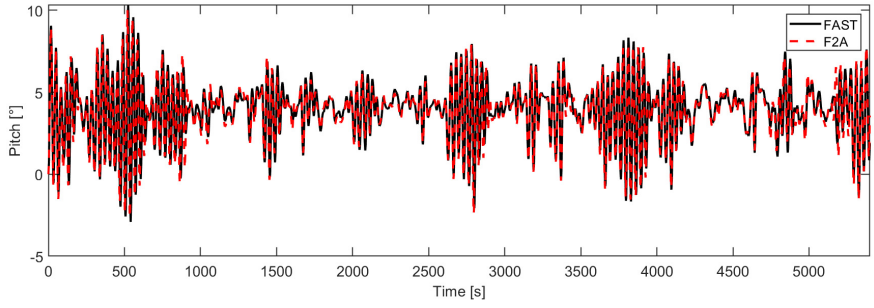
(**b**) Platform Sway



(**c**) Platform Heave

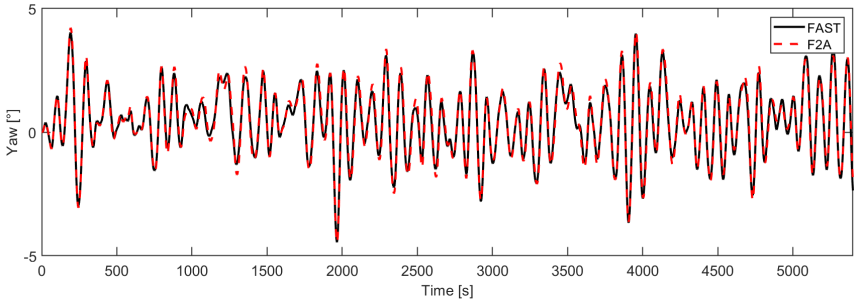


(**d**) Platform Roll



(**e**) Platform Pitch

Figure 5. *Cont.*



(**f**) Platform Yaw

Figure 5. Comparison of six-degree of freedom motion responses of the floating platform.

4.2. Calculation Conditions

Based on the results, the parameter settings for all array models are shown in Table 4. Additionally, a new free decay test was conducted using the F2A method to calculate the natural periods of the platform's six degrees of freedom after the introduction of the wind turbine, as shown in Table 5. It can be observed that after the wind turbine is introduced, the heave natural period of the platform remains unchanged, while the surge, roll, and yaw natural periods slightly decrease. The roll and pitch natural periods exhibit the most significant change, nearly doubling.

Table 4. Parameter settings for each array model.

Parameter	Value
PTO Stiffness/(N/m)	5×10^3
PTO Damping/(Ns/m)	3×10^5
End stop spring Stiffness/(N/m)	1×10^7
End stop spring Space/m	2

Table 5. Six degrees of freedom natural period of floating platform with wind turbine.

	Surge	Sway	Heave	Roll	Pitch	Yaw
Natural Period (s)	177.2	179.1	20.1	29.7	29.7	100.1

Subsequently, to analyze the changes in the motion response of the combined power-generation platform after the introduction of the wind turbine in detail, considering the wave scatter probability in the northern South China Sea, the analysis selected irregular waves based on the JONSWAP spectrum with a wave direction of 0°. The calculation conditions are shown in Table 6 below. Among them, LC-W1, LC-W2, and LC-W3 assess the impact of wind speed on the combined power -generation platform, with wind speeds selected according to the cut-in, rated, and cut-out wind speeds of the turbine [30]. LC-P1, LC-P2, and LC-P3 examine the impact of the spectral peak period of waves on the platform, with a period interval of 3 s. LC-O1, LC-O2, and LC-O3 represent three different operational conditions of the combined power-generation platform, with parameters chosen to closely match actual sea conditions, reflecting the relationship between significant wave height, spectral peak period, and wind speed. Lastly, LC-E represents the survival condition of the combined power-generation platform, with the wind turbine shut down and the PTO device locked, to evaluate its safety performance under extreme sea conditions.

Table 6. Calculation conditions.

Calculation Conditions		Significant Wave Height (m)	Spectral Peak Period (s)	Turbulent Wind Speed (m/s)
LC-W	1	1.5	7.5	4
	2	1.5	7.5	11.4
	3	1.5	7.5	25
LC-P	1	1.5	4.5	11.4
	2	1.5	7.5	11.4
	3	1.5	10.5	11.4
LC-O	1	2.2	8	10.3
	2	3.04	9.5	13.9
	3	4.29	10	17.9
LC-E		10.9	16	44

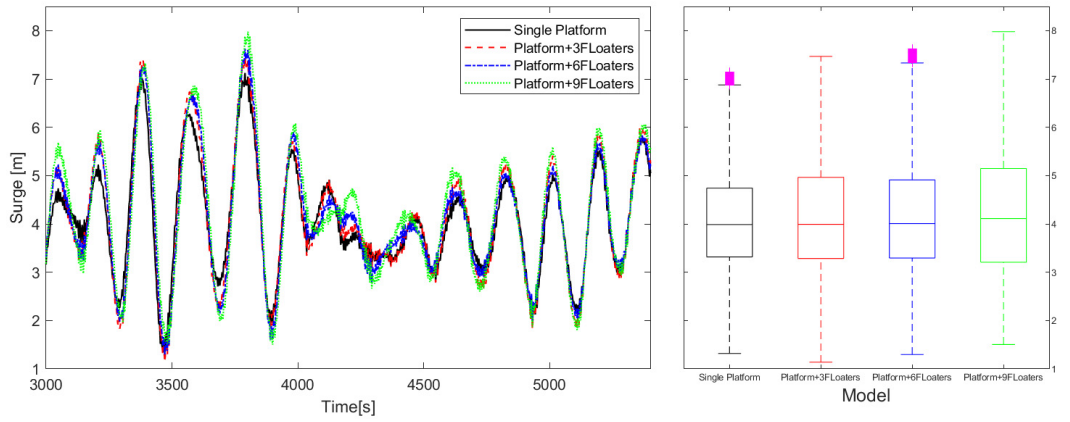
4.3. Analysis of Fully Coupled Dynamic Response Parameters of Wind-Wave Combined Power-Generation Platform

4.3.1. Dynamic Response Analysis of Wind-Wave Combined Power-Generation Platform under Different Wind Speeds

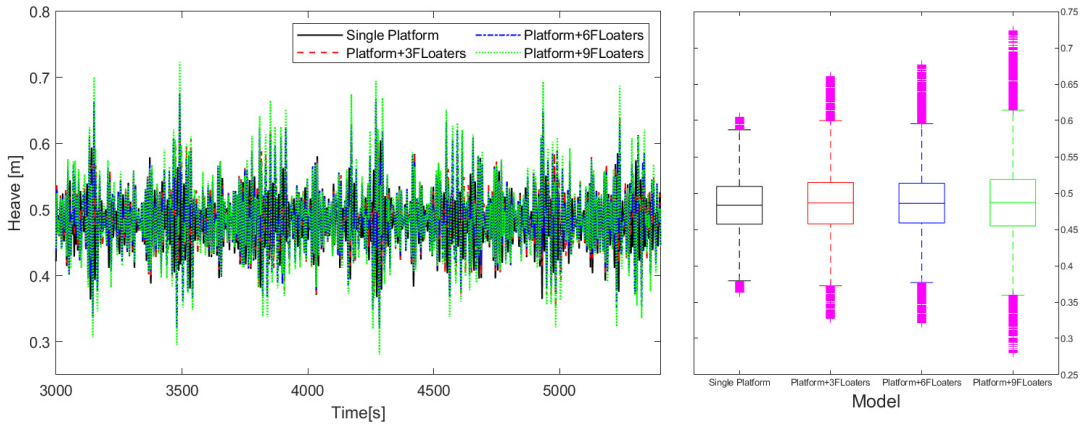
As shown in Figures 6–8, the motion response comparison is presented for the platform with different floater array configurations under various wind speeds. The left side of each figure displays the time history curves, while the right side shows the box plots of the responses during the observed period. Firstly, considering the overall trend, the platform's motion tendency is minimally affected by the floater array across the three different wind speeds, and the mean value of the motion remains largely unchanged, as indicated by the nearly constant median in the box plots. Further analysis of the three degree of freedom motion response under a wind speed of 4 m/s reveals that, in terms of motion extremes, the surge and heave motion extremes increase with the number of floaters. Notably, the heave motion extreme shows the most significant change, increasing from 0.24 m under a single platform to 0.43 m under a nine-floater array, a change of over 50%. In contrast, the pitch motion is less influenced by the floater array, with no significant changes in either its extreme or mean values. However, as the wind speed increases, although the heave motion response continues to follow the previously described pattern, the mean value of the platform's surge motion gradually increases with the number of floaters, indicating a progressive deviation from the mooring's original position. This suggests that as wind speed increases, the wind overturning moment gradually impacts the platform's horizontal motion. At the same time, the pitch motion of the platform decreases with the increase in the number of floaters, reflecting the damping effect of the oscillating floaters on the platform's pitch motion.

To further examine the impact of varying wind speeds on platform motion response, Figure 9 shows the motion response of a single platform under different wind speeds. It can be observed that the platform's motion response is not directly proportional to the wind speed. Instead, the platform exhibits the largest interquartile range, indicating greater motion amplitude, at the rated wind speed. This phenomenon primarily occurs because, when the wind speed exceeds the rated wind speed of the turbine, the pitch angle of the turbine blades increases, reducing the windward area of the turbine, which in turn decreases the thrust on the turbine and results in a gradual reduction in the platform's motion amplitude. Additionally, there is a significant variation in the mean motion of the platform under different wind speeds. The platform's maximum surge displacement is 21.8 m, and the maximum pitch displacement is 3.9°, both occurring at the rated wind speed. The maximum heave displacement is 0.48 m, occurring at the cut-in wind speed.

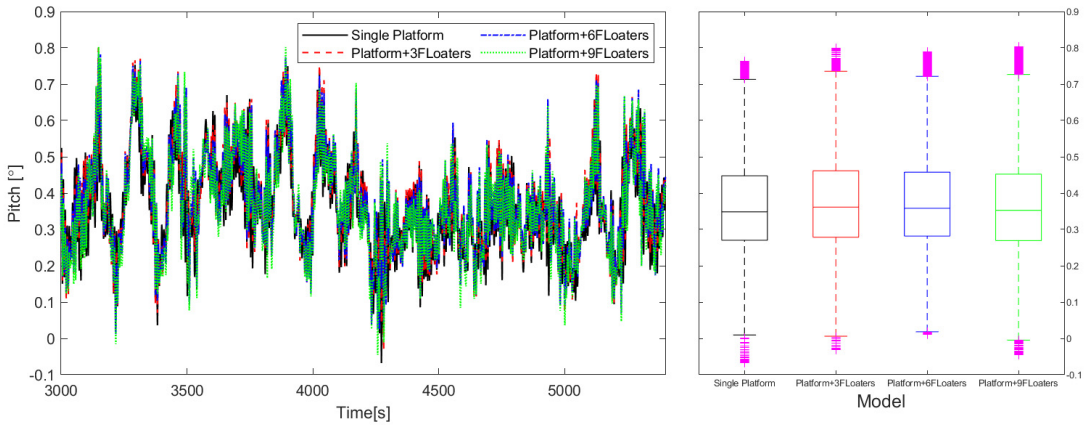
Therefore, overall, the rated wind speed remains in the condition with the greatest impact on platform motion response, which requires close attention under actual sea conditions.



(**a**) Platform Surge

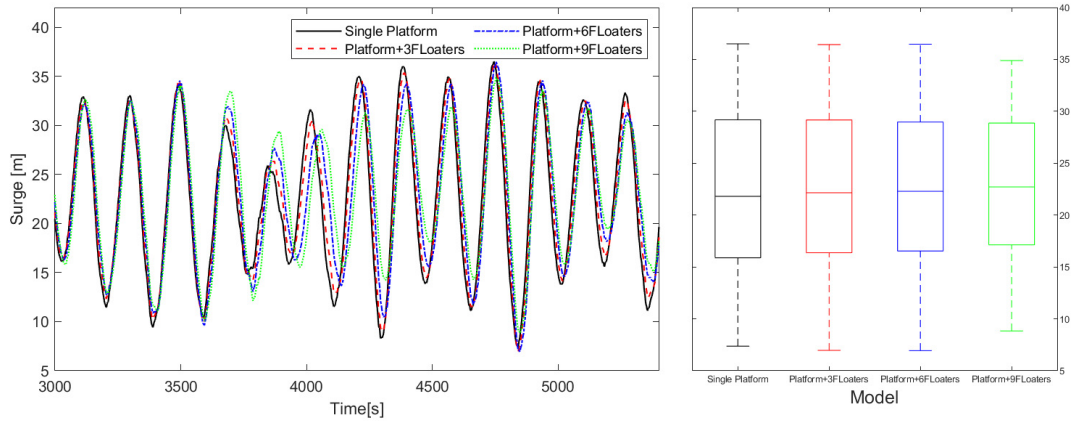


(**b**) Platform Heave

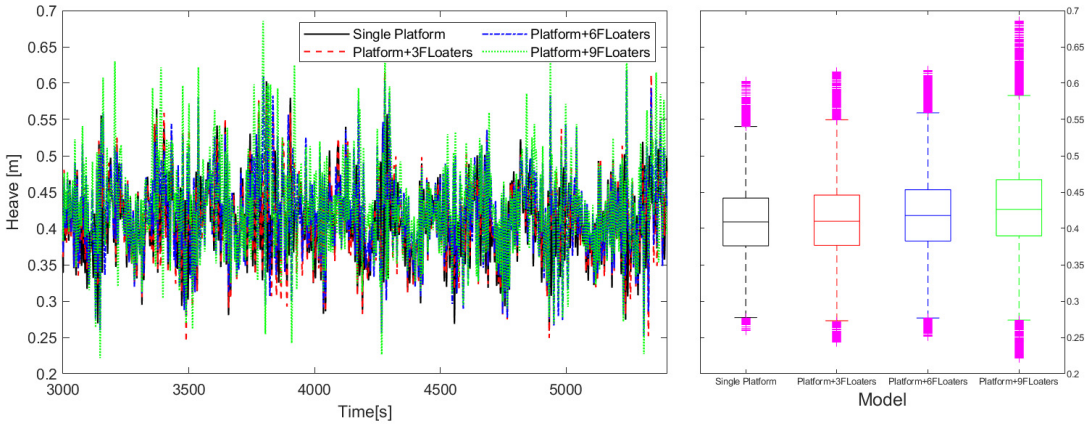


(**c**) Platform Pitch

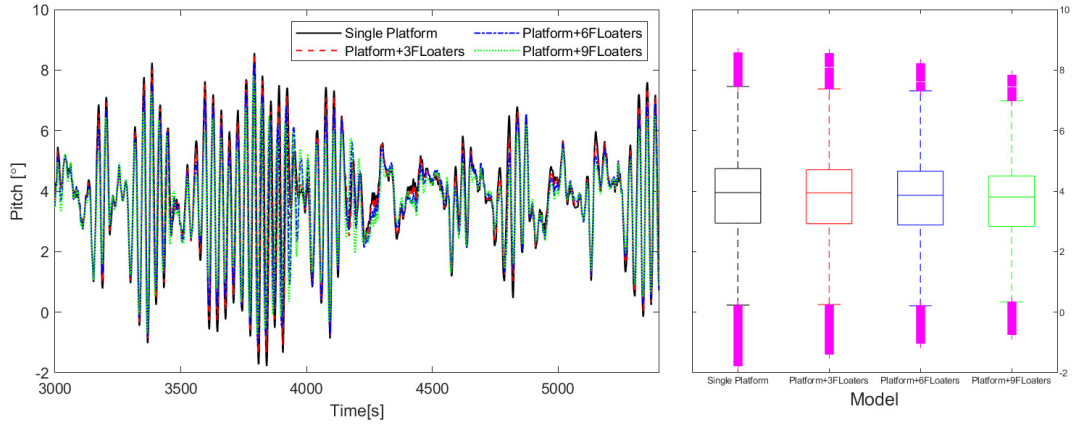
Figure 6. Comparison of platform motion response under different array models. (Wind speed = 4 m/s).



(**a**) Platform Surge

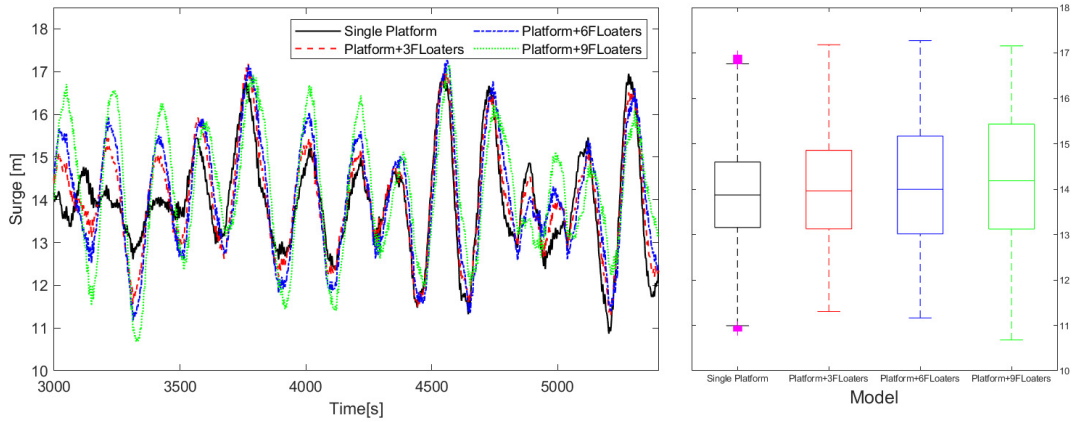


(**b**) Platform Heave

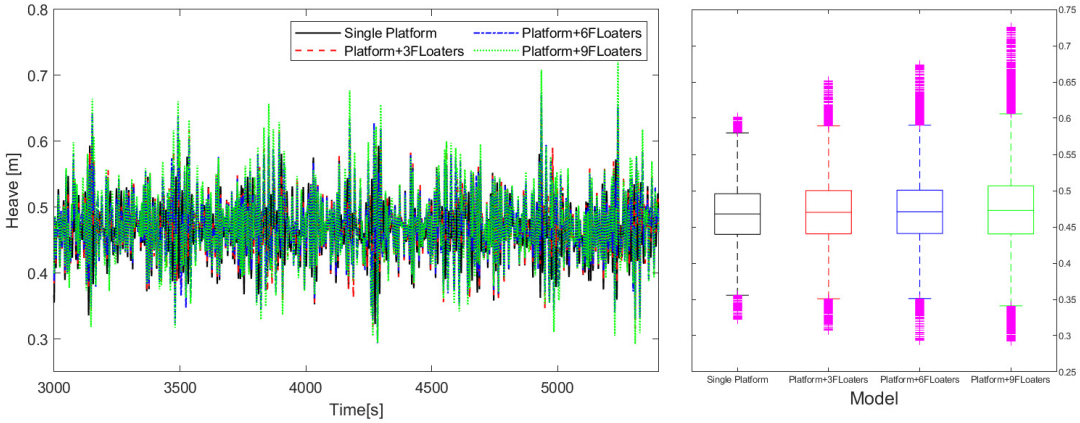


(**c**) Platform Pitch

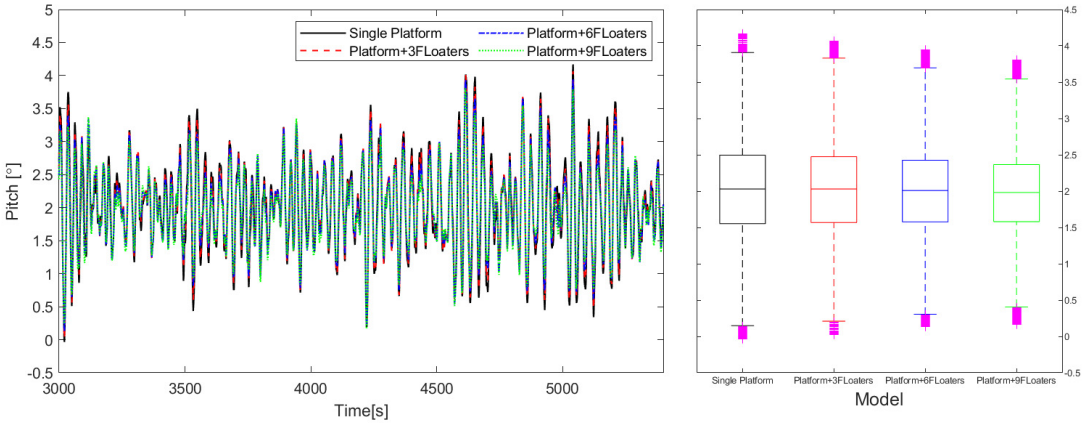
Figure 7. Comparison of platform motion response under different array models. (Wind speed = 11.4 m/s).



(**a**) Platform Surge



(**b**) Platform Heave

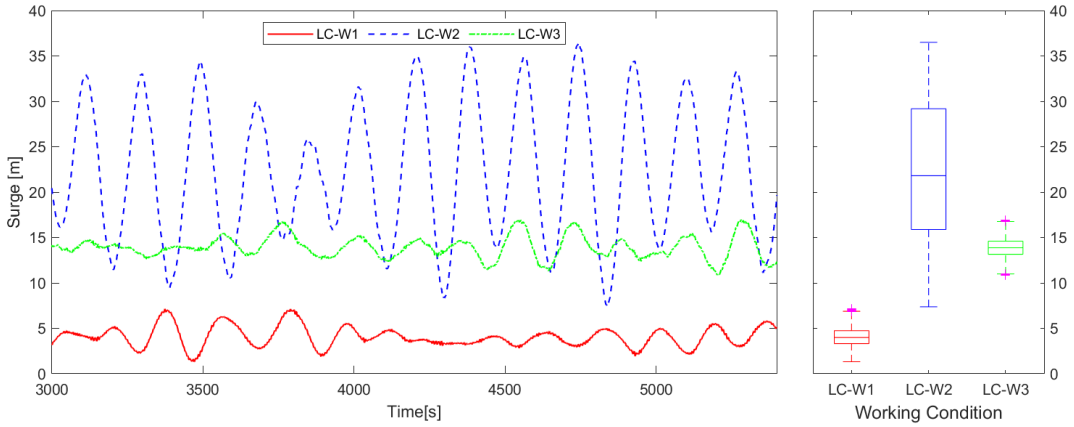


(**c**) Platform Pitch

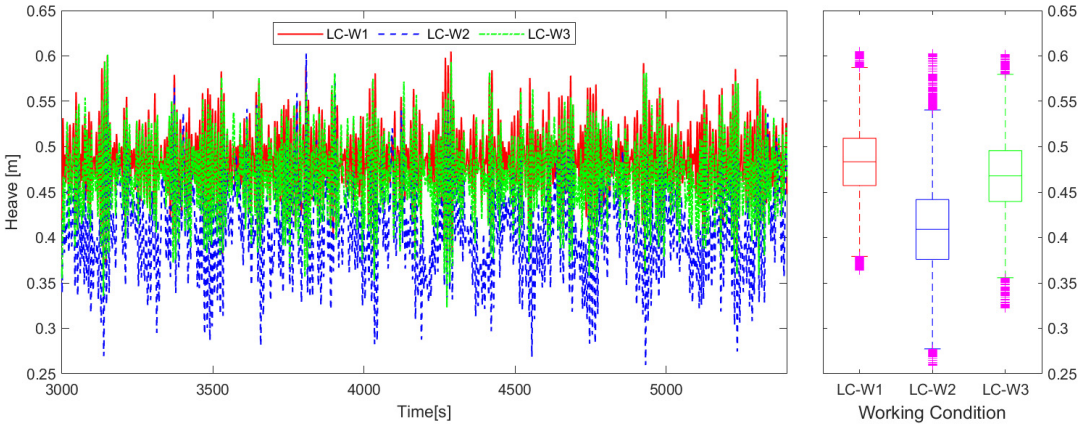
Figure 8. Comparison of platform motion response under different array models. (Wind speed = 25 m/s).

Subsequently, a comparison of the mooring responses of the combined wind-wave power-generation platform was conducted, focusing on the analysis of fairlead tension and catenary length variations. Initially, the impact of different floater arrays on the mooring system was considered at the wind speed of 11.4 m/s, where the motion response was the largest, as shown in Figure 10. It is evident that due to the mooring arrangement and wave direction, floaters 2 and 3 experience greater forces. Further comparison revealed

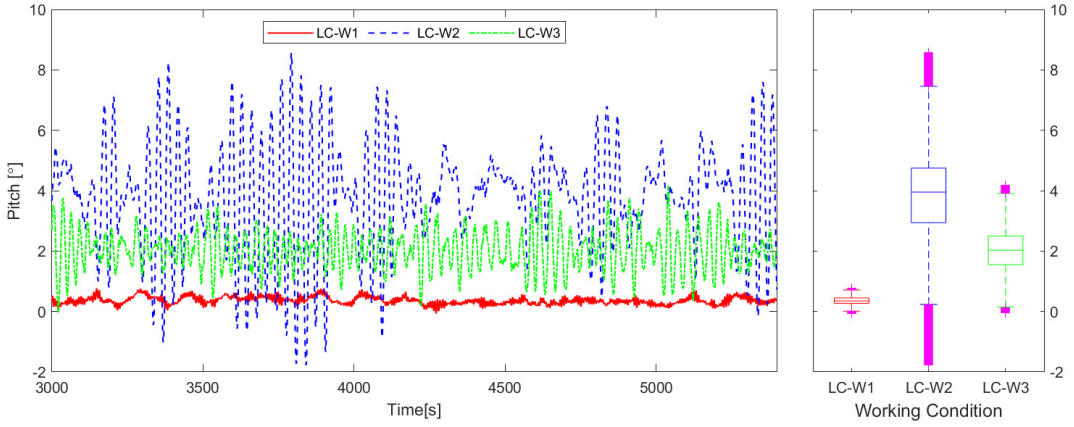
that the maximum values of cable tension and laid length tend to decrease gradually as the number of floaters increases, indicating that oscillating floaters can help enhance the mooring capacity of floating wind turbines at certain wind speeds.



(**a**) Platform Surge

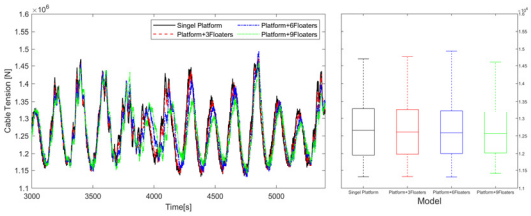


(**b**) Platform Heave

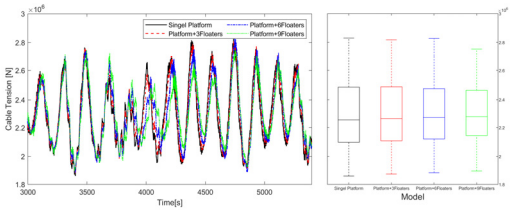


(**c**) Platform Pitch

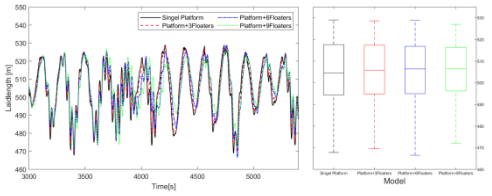
Figure 9. Comparison of motion responses of the combined power-generation platform under different wind speeds.



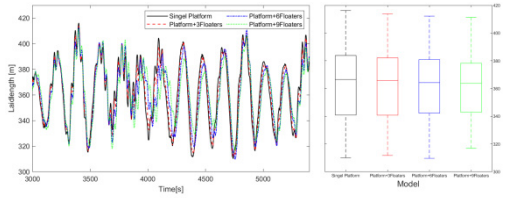
(**a**) Cable 1 tension.



(**b**) Cable 2/3 tension.



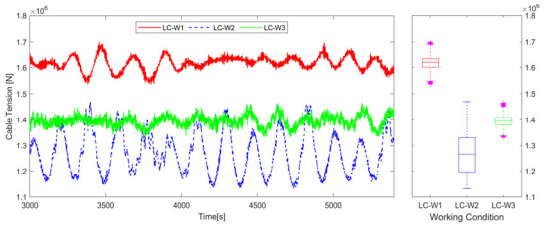
(**c**) Cable 1 laid length.



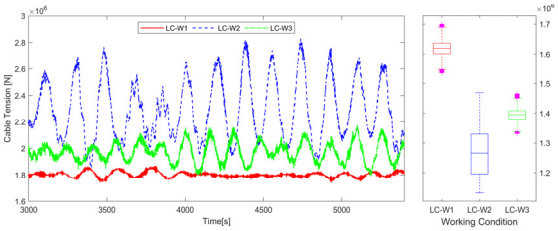
(**d**) Cable2/3 laid length.

Figure 10. The Impact of different floater arrays on the dynamic mooring response. (Wind speed = 11.4 m/s.)

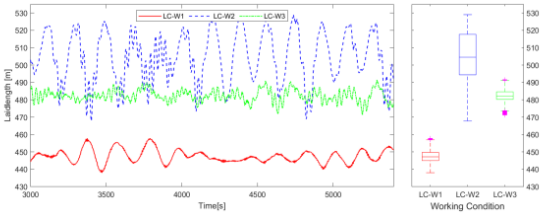
Next, the mooring responses of a single platform under different wind speeds were compared. As shown in Figure 11, it found that the trend of cable tension and laid length variations in the mooring lines under different wind speeds is highly consistent with the platform's surge motion response. Overall, the greatest variation in amplitude occurs at the rated wind speed, followed by the cut-out wind speed, and lastly, the cut-in wind speed. Additionally, due to the changes in force caused by the variations in motion amplitude, the maximum cable tension is highest at the rated wind speed, while the corresponding minimum laid length is the shortest.



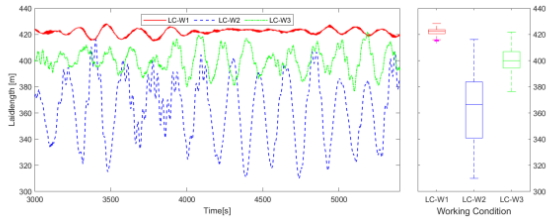
(**a**) Cable 1 tension.



(**b**) Cable2/3 tension.



(**c**) Cable 1 laid length.

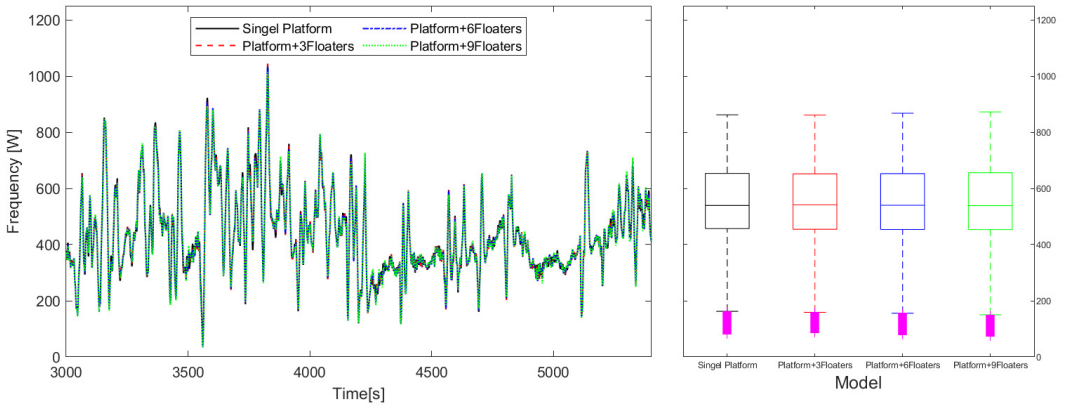


(**d**) Cable 2/3 laid length.

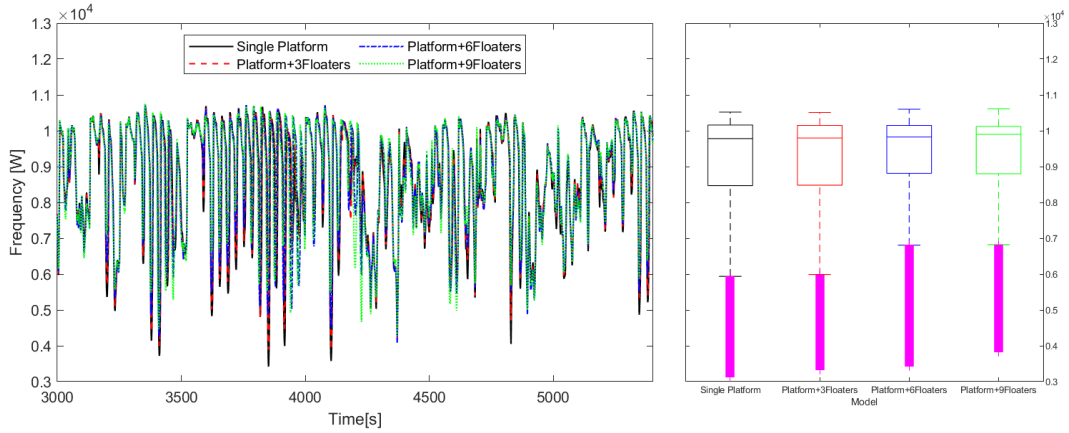
Figure 11. Comparison of mooring responses of a single platform under different wind speeds.

Further analysis of the variation in system power generation under different wind speeds and array models begins with the analysis of the power generation of the upper wind turbine. Figure 12 shows a comparison of wind turbine power generation when different arrays of oscillating floats are arranged on the floating platform under various wind speeds. It is evident that regardless of the number of oscillating floats arranged, the average power generation of the wind turbine remains almost unchanged. Thus, it can be

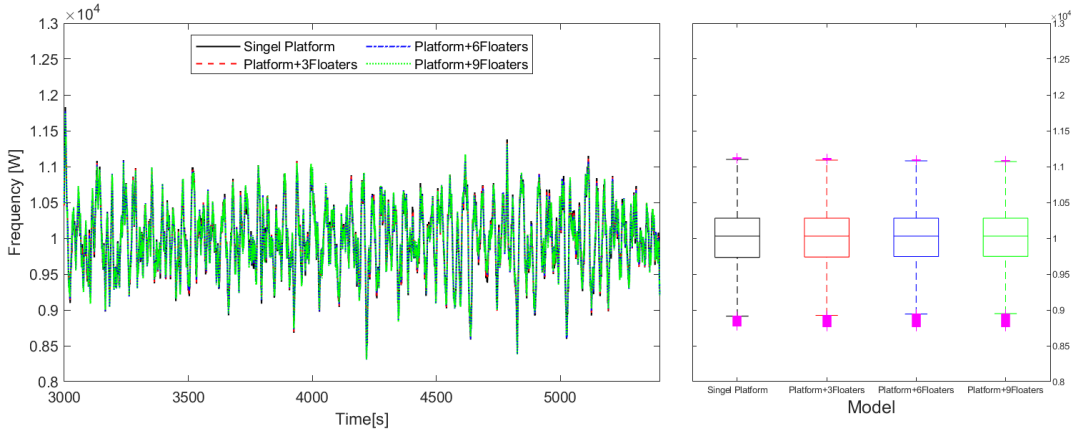
concluded that the oscillating floats do not affect the power-generation performance of the upper wind turbine.



(**a**) LC-W1 operating wind speed = 4 m/s.



(**b**) LC-W2 operating wind speed = 11.4 m/s.



(**c**) LC-W3 operating wind speed = 25 m/s.

Figure 12. Variation in wind turbine power generation under different array models.

Comparing the power generation under different wind speeds, as shown in Figure 13, it can be observed that the wind turbine's power generation is most unstable under turbulent wind at rated wind speed, with the minimum power dropping to 3.3 MW. In contrast, at the cut-out wind speed, the turbine's power generation remains consistently around 10 MW. This instability under rated wind speed is clearly due to the randomness of tur-

bulent wind, which causes a certain lag in the turbine's pitch control, leading to greater fluctuations in power generation.

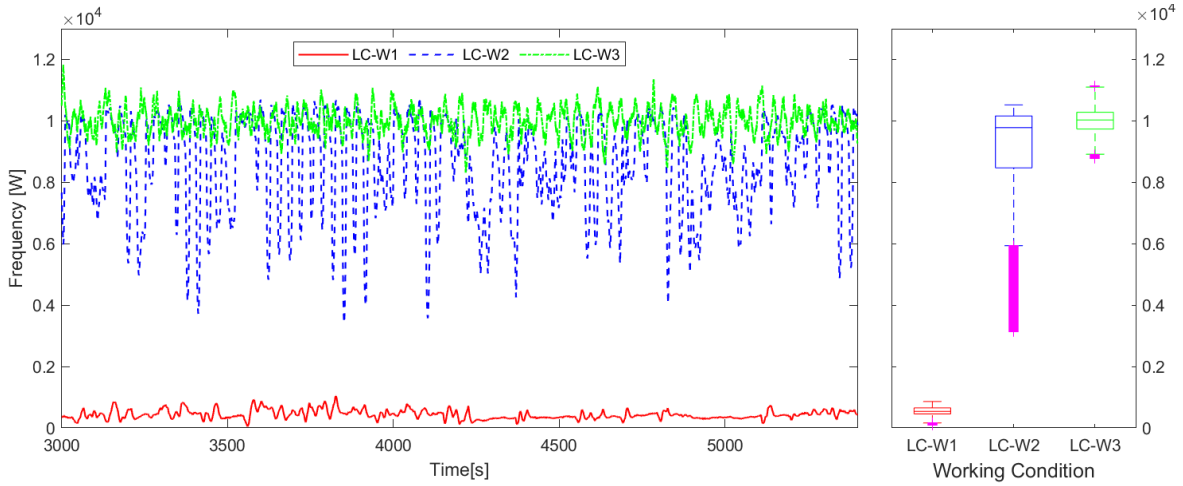
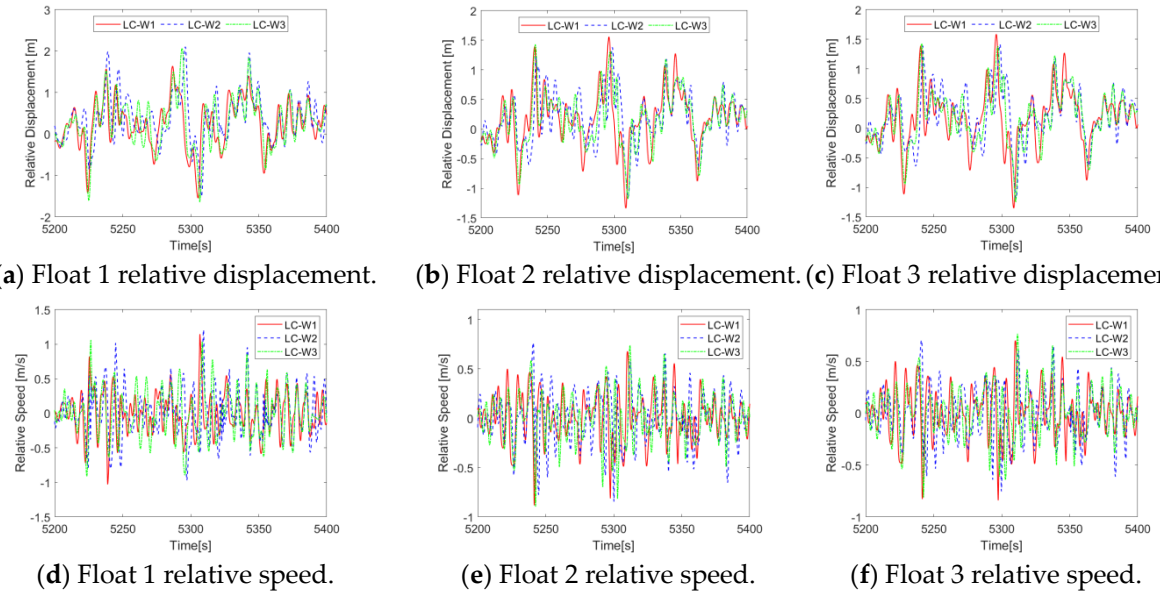


Figure 13. Variation in wind turbine power generation under different wind speeds.

For the wave energy device, calculating its power generation requires considering the relative motion between the oscillating floats and the platform. Figure 14 presents the variation curves of relative displacement and velocity between each float and the platform for a three-float array under different wind speeds. Under the constraints of the end-stop system, the relative displacement between the floats and the platform rarely exceeds 2 m, and the relative velocity remains within 1.5 m per second. Additionally, due to the symmetry of the model, the motion responses of floats 2 and 3 tend to be consistent. The relative motion trends of the floats are generally consistent under different wind speeds.



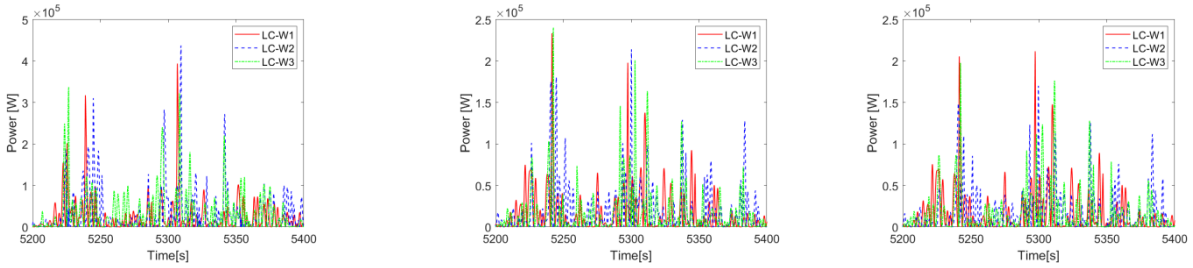
(**a**) Float 1 relative displacement. (**b**) Float 2 relative displacement. (**c**) Float 3 relative displacement.

(**d**) Float 1 relative speed. (**e**) Float 2 relative speed. (**f**) Float 3 relative speed.

Figure 14. The relative displacement and velocity variations between each float and the floating platform in the three-float array.

Further, based on the relative velocity, the instantaneous power generation of each float is calculated, as shown in Figure 15. It found that the instantaneous power generation of floats 2 and 3 exhibits some differences, which is likely due to the coupling between the platform's roll motion and the floats' heave motion, causing inconsistent changes in

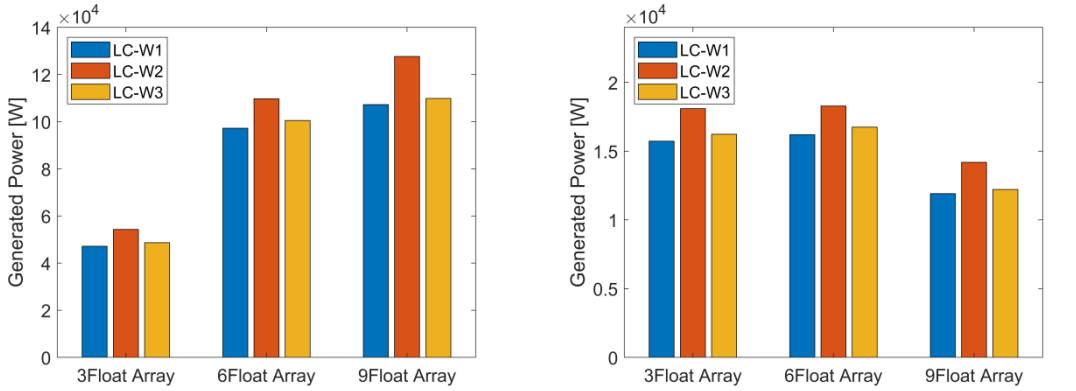
relative velocity on either side of the platform. Additionally, under different wind speeds, the power-generation performance of float 1 generally surpasses that of floats 2 and 3, as indicated by its instantaneous power peaks, which are roughly double those of the other two floats.



(**a**) Float 1 instantaneous power. (**b**) Float 2 instantaneous power. (**c**) Float 3 instantaneous power.

Figure 15. The instantaneous power generation variations of each float in the three-float array.

A comprehensive statistical analysis was conducted to examine the total instantaneous power generated by each array model under varying wind speeds over a 5400 s period. The average values were calculated and illustrated in the bar chart in Figure 16a. The results indicate that the total power generation across different wind speeds does not vary significantly, with the highest power generation still observed at the rated wind speed. This is likely due to the platform's enhanced motion response at this wind speed, which amplifies the relative motion coupled with the floats. Additionally, a non-dimensional analysis was performed to evaluate the average power generation of individual floats within different array configurations, as depicted in Figure 16b. Overall, the six-float array demonstrated superior performance, while the nine-float array exhibited the poorest results. Therefore, to maximize the energy capture potential of each oscillating float, simply increasing the number of floats beyond a certain threshold may not be the most effective strategy.



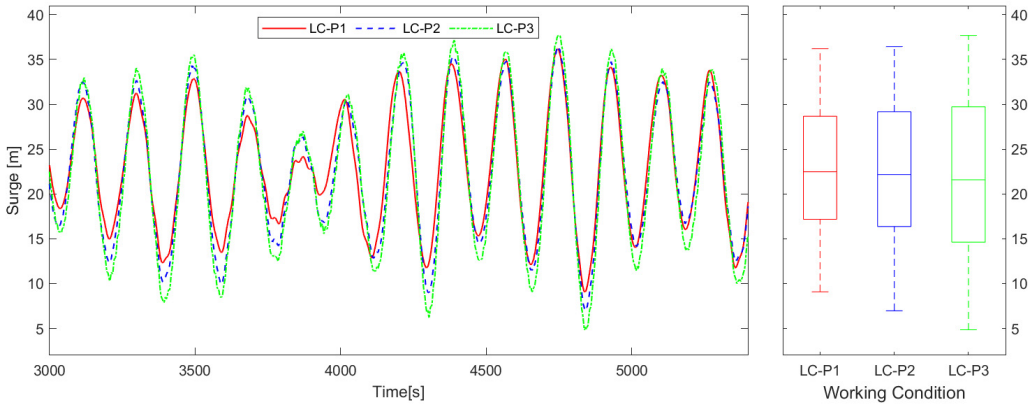
(**a**) Total power generation. (**b**) Single-float average power generation.

Figure 16. Comparison chart of power generation under different array layouts and wind speeds.

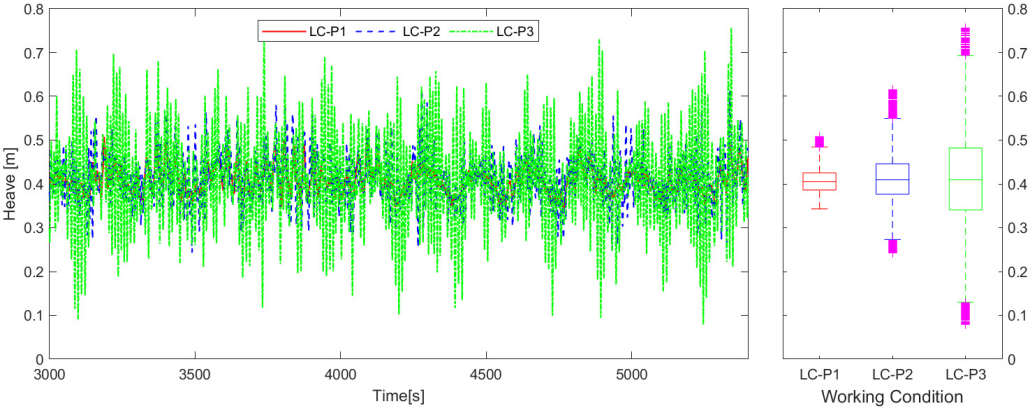
4.3.2. Dynamic Response Analysis of Wind-Wave Combined Power

Figure 17 shows the time history of the motion response of a three-float array -type combined power-generation platform under three different spectral peak periods. The results indicate that the platform's surge amplitude increases with the spectral peak period. This is largely due to the surge natural period being relatively long, so the closer the spectral peak period is to the surge natural period, the greater the resulting motion response. Furthermore, the heave amplitude shows a more significant increase as the spectral peak period approaches the heave natural period. In contrast, the pitch amplitude and the average motion response across all three degrees of freedom remain largely unchanged by

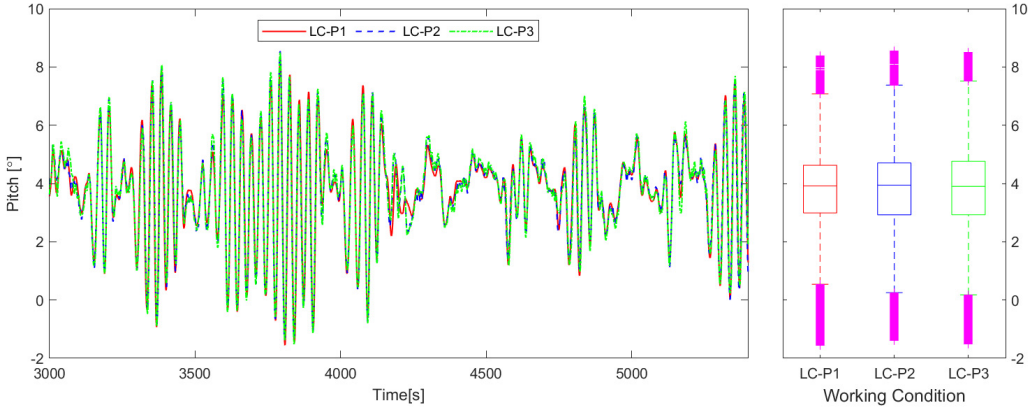
variations in the spectral peak period, indicating minimal sensitivity. This suggests that the motion offset in each degree of freedom is mainly influenced by wind loads on the upper structure, while the spectral peak period primarily affects the amplitude of the response.



(**a**) Platform Surge



(**b**) Platform Heave

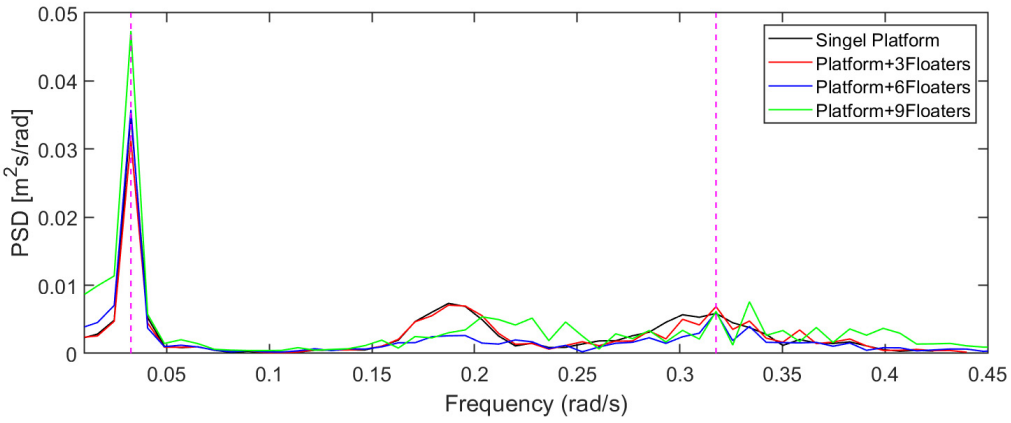


(**c**) Platform Pitch

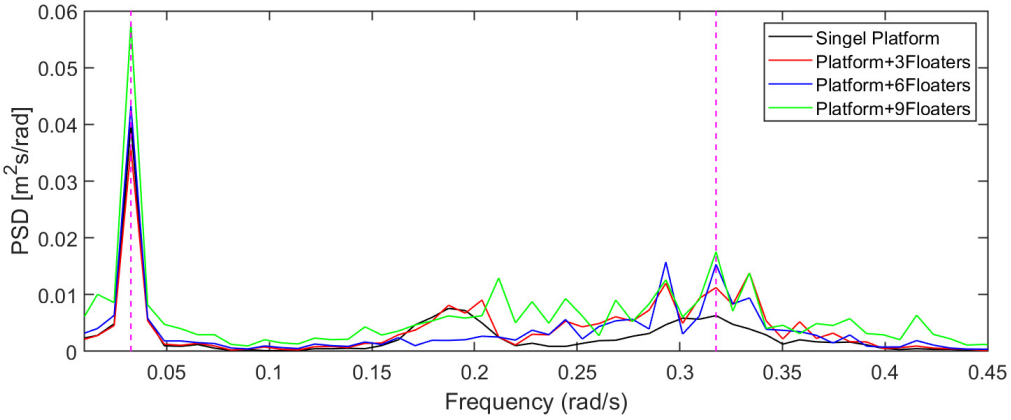
Figure 17. Comparison of motion responses of a three-float array type combined power-generation platform under different spectral peak periods.

Subsequently, a power spectral analysis of the heave motion of the floating platform under different array models was conducted, as shown in Figure 18. In the figure, all frequencies corresponding to common peak values are marked. It can be observed that, for

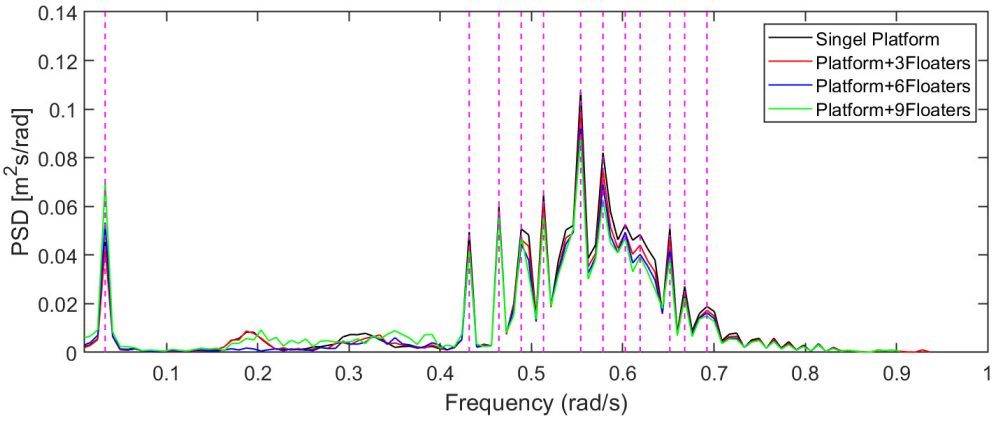
all array models and wave frequencies, the floating platform exhibits a significant peak at a low frequency of 0.0326 rad/s. This frequency is very close to the second-order mode of the wind turbine tower, which is at 0.0339 rad/s, suggesting a strong coupling effect between the tower and the platform's heave motion.



(**a**) 4.5 s.



(**b**) 7.5 s.



(**c**) 10.5 s.

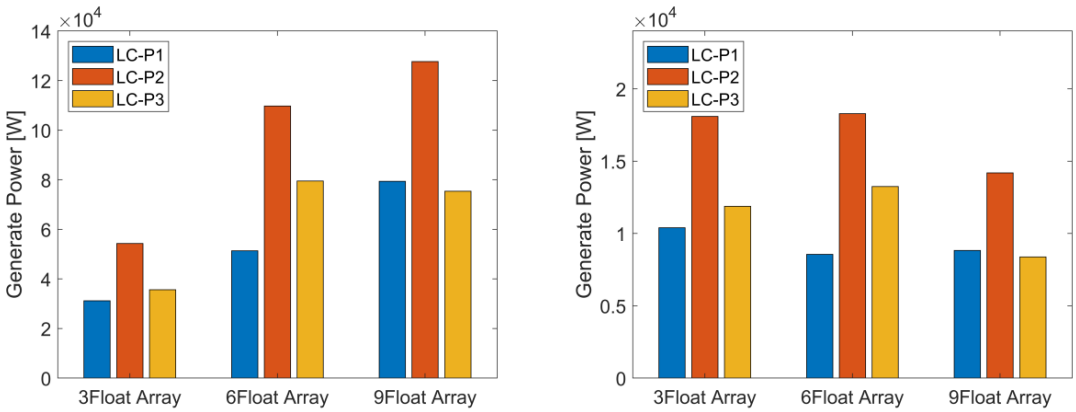
Figure 18. Comparison of heave power spectra of floating platforms under different array configurations.

Additionally, it was found that under wave periods of 4.5 s and 7.5 s, the power spectrum shows a secondary peak at 0.318 rad/s. This peak corresponds to the natural frequency of the platform's heave motion, indicating that at these wave frequencies, the heave motion of the floating platform is primarily influenced by its own resonant frequency.

Furthermore, the spectrum gradually converges to zero at 0.45 rad/s, implying that the heave motion is minimally affected by wave frequency.

Lastly, examining the power spectral curve for a 10.5 s wave period reveals multiple peaks in the frequency range from 0.4 rad/s to 0.7 rad/s, indicating the presence of coupling between the heave motion and multiple modes. The highest peak within this range occurs at 0.55 rad/s, which is very close to the wave frequency, suggesting that the platform's motion is significantly influenced by the wave frequency currently.

Finally, a comparison of the total power generation of the oscillating floats under different array configurations and spectral peak periods was conducted, as shown in Figure 19a. It can be observed that the total power generation is maximized for all three array configurations at the spectral peak period of 7.5 s, the average power generation per float was analyzed, as shown in Figure 19b. The six-float array still produces the highest average power per float, further corroborating the conclusions drawn in the previous section.

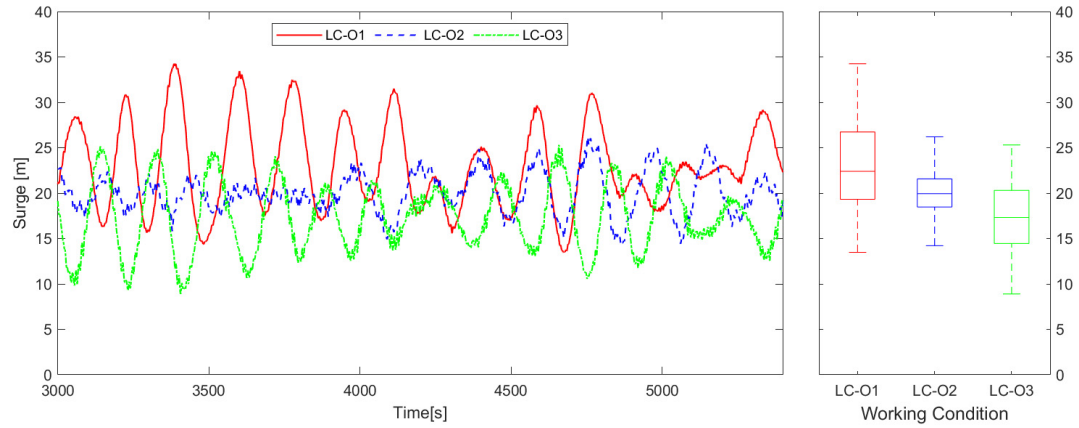


(**a**) Total power generation. (**b**) Single-float average power generation.

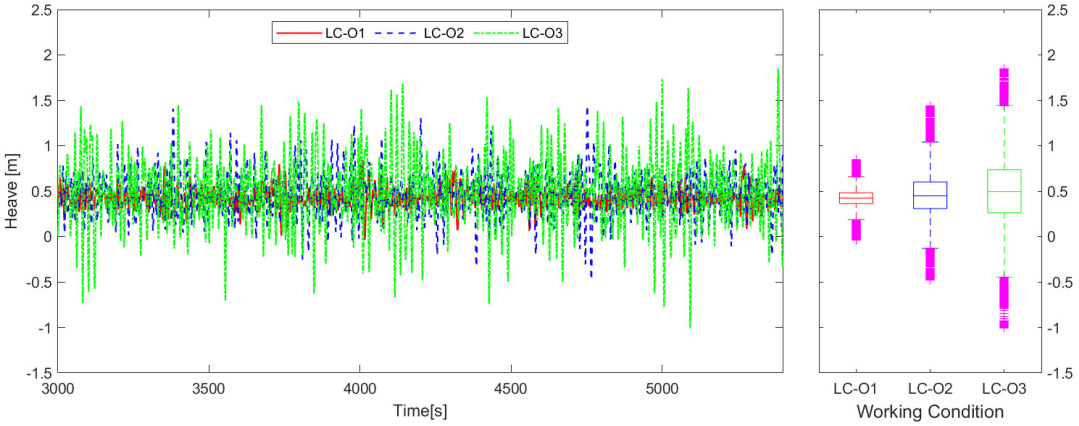
Figure 19. Comparing power generation under different array configurations and spectral peak periods.

4.4. Working Condition Motion Response Analysis

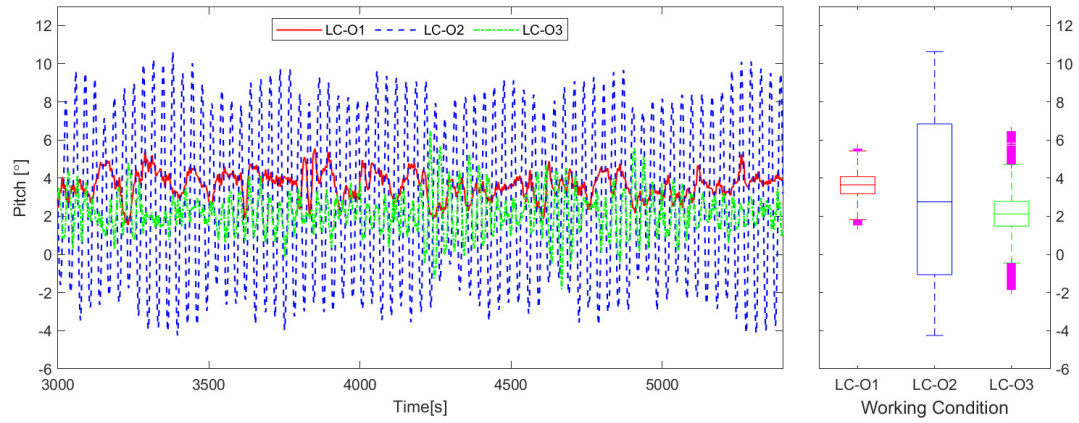
Based on the previous parameter analysis, the motion response of the combined power-generation platform under different operating conditions was investigated. The selection of these conditions considered the interrelationships between wind speed, wave height, and wave period under real sea conditions, to explore the optimal sea state for the comprehensive performance of the combined power-generation platform. As shown in Figure 20, the motion response of the combined power-generation platform under different conditions for the three-float array is compared. It can be observed that as the sea state intensifies, the heave motion amplitude and its extreme values of the platform gradually increase, reaching a maximum of 1.5 m. However, the surge displacement gradually decreases, which is like the previous conclusions. This can be attributed to the increase in wind speed leading to an increase in the blade pitch angle of the wind turbine, thereby reducing the wind-induced tilting moment and resulting in a smaller surge displacement. An interesting phenomenon is the sudden increase in the pitch motion amplitude of the platform under the second operating condition, with the maximum amplitude reaching 7°. This could be due to the wave period at this condition coinciding with a relevant mode of the wind turbine, causing resonance and, consequently, a significant motion response.



(**a**) Platform Surge



(**b**) Platform Heave



(**c**) Platform Pitch

Figure 20. Comparison of motion responses of the combined power-generation platform under different operating conditions for the three-float array.

Further comparison of the wind turbine's power generation under different operating conditions is shown in Figure 21. Due to the resonance phenomenon and the randomness of turbulent wind, the power generation of the wind turbine under LC-W2 is highly unstable, with the lowest power output at 3.9 MW. In contrast, the power generation under the other two conditions is relatively stable. LC-W1 has a lower power output due to the inability to reach the rated wind speed, while LC-W3 remains stable around 10 MW.

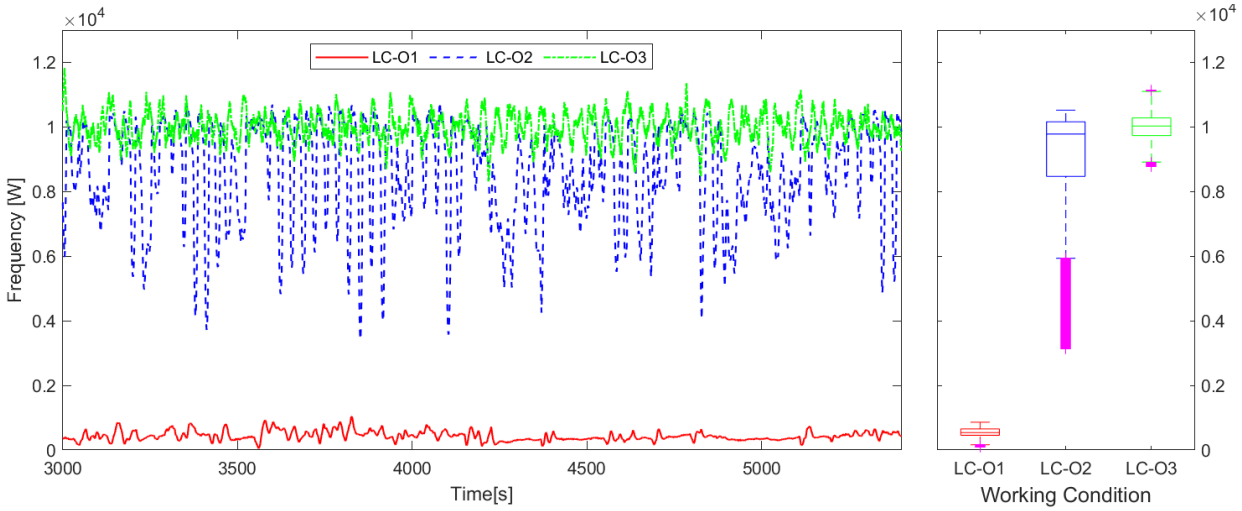
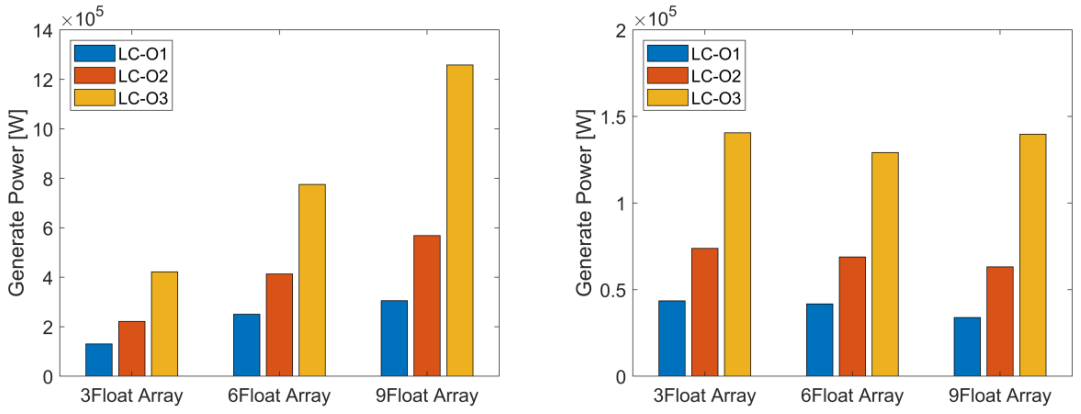


Figure 21. Comparison of wind turbine power generation on the combined power-generation platform under different operating conditions.

Finally, the total power generation of the oscillating floats and the average power generation per float under different array configurations and operating conditions were also analyzed, as shown in Figure 22. As wave height increases, the power generation of the floats also gradually rises. This suggests that compared to wave period, the power generation of the lower wave energy conversion devices is more significantly influenced by wave height. Additionally, it can be noted that since the wave frequency exceeds the optimal power-generation frequency, the average power generation per float across the three array configurations shows minimal variation.



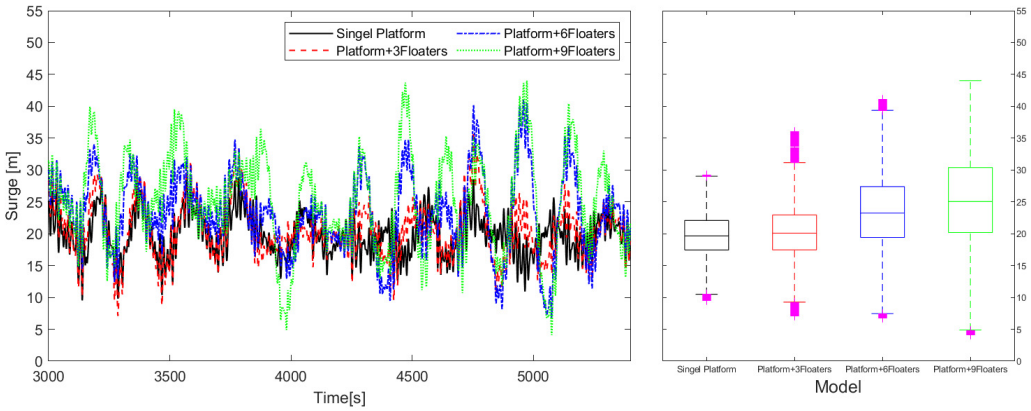
(**a**) Total power generation. (**b**) Single-float average power generation.

Figure 22. Comparison of power generation u different array configurations and operating conditions.

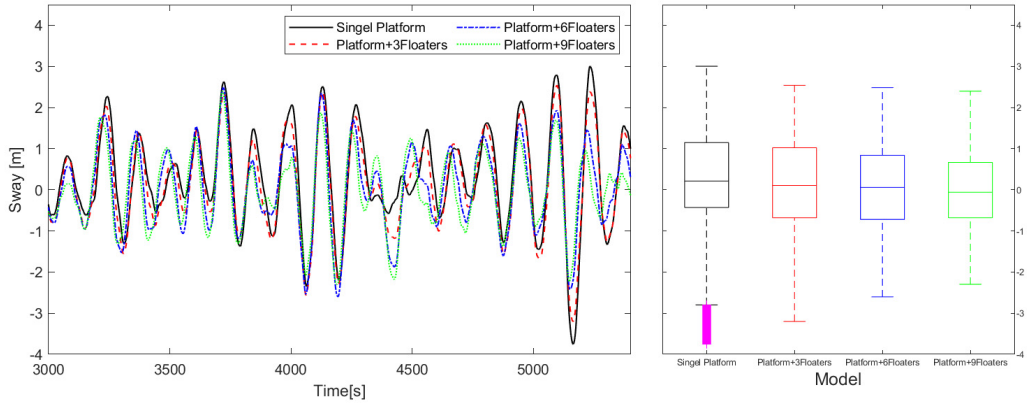
4.5. Survival Condition Motion Response Analysis

In the final section, the safety performance of the combined power-generation platform under survival conditions is verified. Due to excessive wind speeds and wave heights, the wind turbine must be adjusted to feathering mode, while the yaw and blade rotational degrees of freedom of the turbine are locked, placing the upper wind turbine in a shutdown state. Additionally, the lower wave energy device must also be locked to ensure that the PTO system is not damaged [31,32]. Figure 23 shows a comparison of the six degrees of freedom motion of the floating platform under different models. It can be observed that under survival conditions, both the pitch and heave motion amplitudes of the floating platform increase as the number of floats increases, especially in heave, where the maxi-

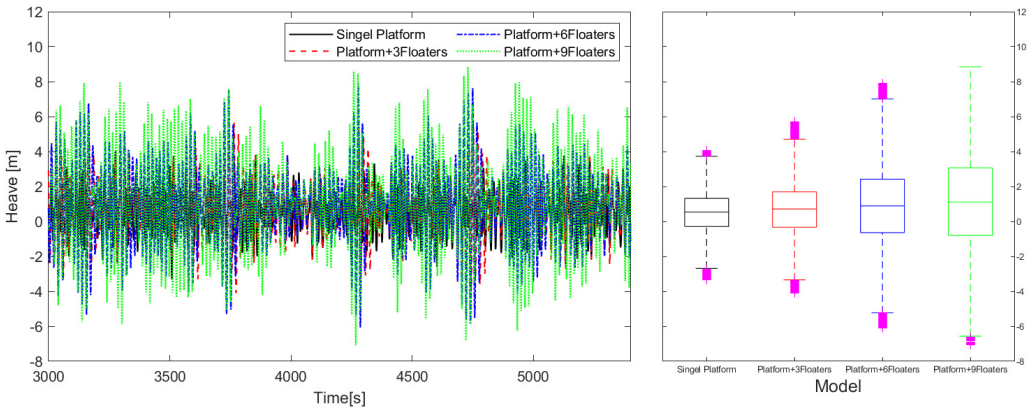
mum amplitude nearly doubles. The motion displacement also gradually increases, with pitch displacement increasing from 20 m to 25 m and heave displacement from 0.5 m to 1 m, which could negatively impact the mooring safety of the system. However, for the platform's other four degrees of freedom, the motion displacement decreases as the number of floats increases, with the most noticeable reduction in roll, from the original 2° to 1.2°. The motion amplitudes generally show a decreasing trend as well, indicating that the introduction of oscillating floats can improve the motion response of the floating platform in sway, roll, pitch, and yaw to some extent.



(**a**) Platform Surge

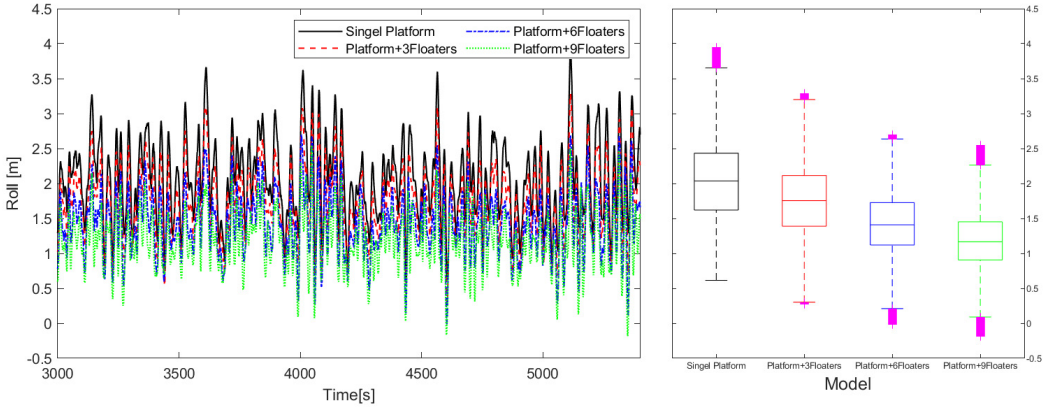


(**b**) Platform Sway

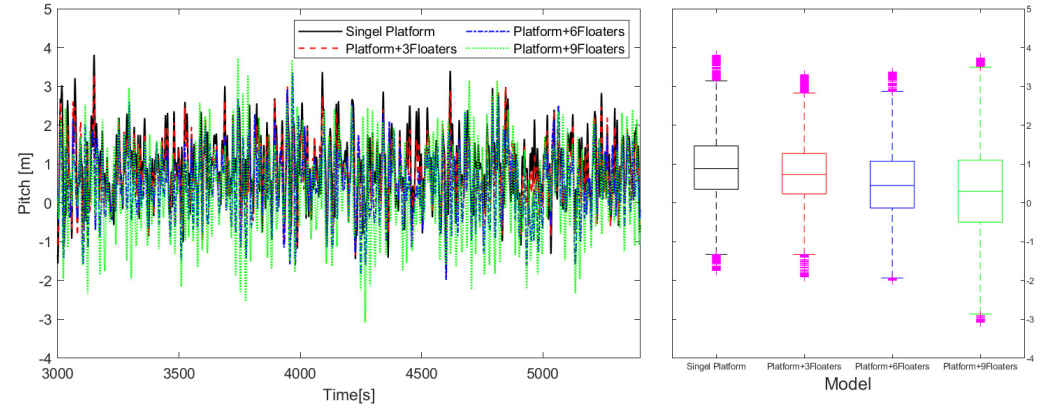


(**c**) Platform Heave

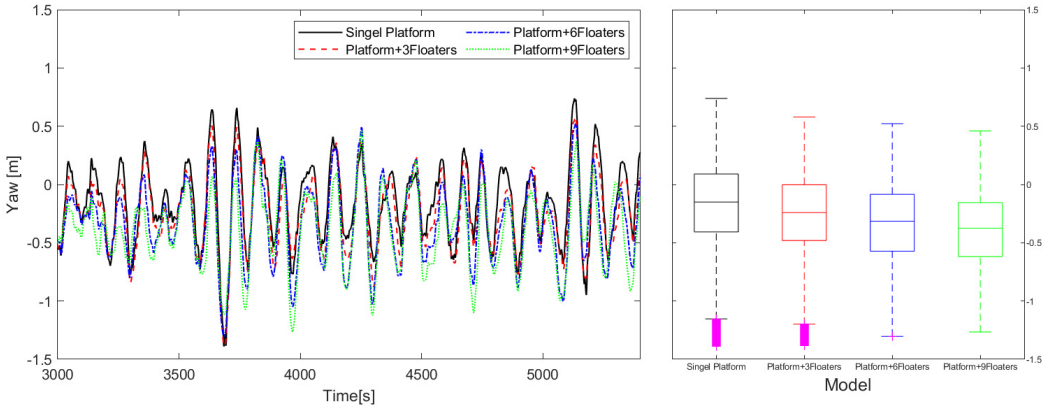
Figure 23. *Cont.*



(**d**) Platform Roll



(**e**) Platform Pitch

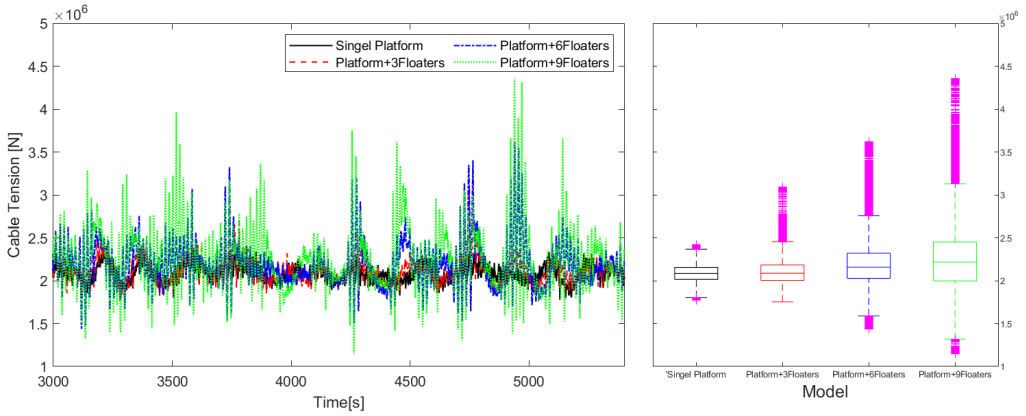


(**f**) Platform Yaw

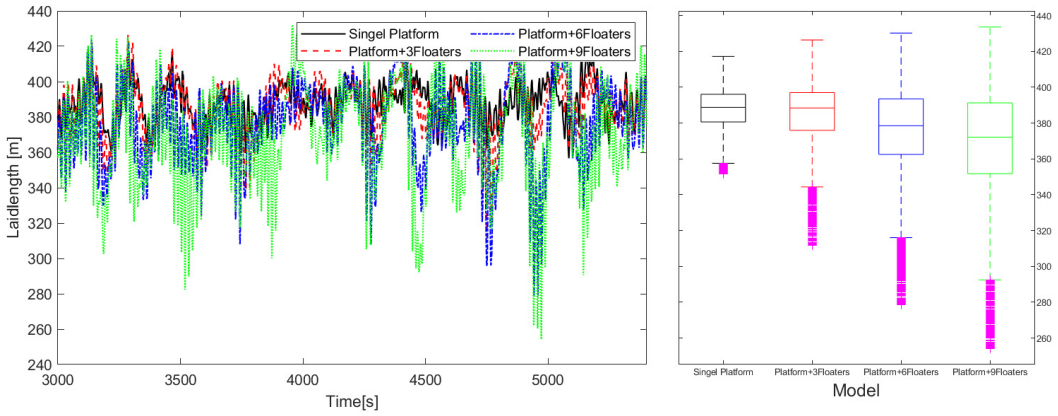
Figure 23. Comparison of six degrees of freedom motion of the floating platform under different models.

Further analysis of the platform's mooring response focuses on cable 2, which is subject to the greatest forces. As shown in Figure 24, the cable tension and laid length of the cable under different models exhibit a trend consistent with the pitch motion of the platform. Specifically, as the number of floats increases, the peak cable tension gradually increases, and the laid length decreases accordingly. The shortest laid length is observed in the combined power-generation platform with a nine-float array, reaching 250 m. Further analysis of anchor force changes, as shown in Figure 25, indicates that the maximum

anchor force occurs at this location, reaching 11.5 N, while the anchor force is almost zero throughout for a single platform. Therefore, for the mooring system, an increase in the number of floats reduces the overall mooring safety of the system.



(**a**) Cable 2 tension.



(**b**) Cable 2 laid length.

Figure 24. Comparison of mooring dynamic response of cable 2 under different models.

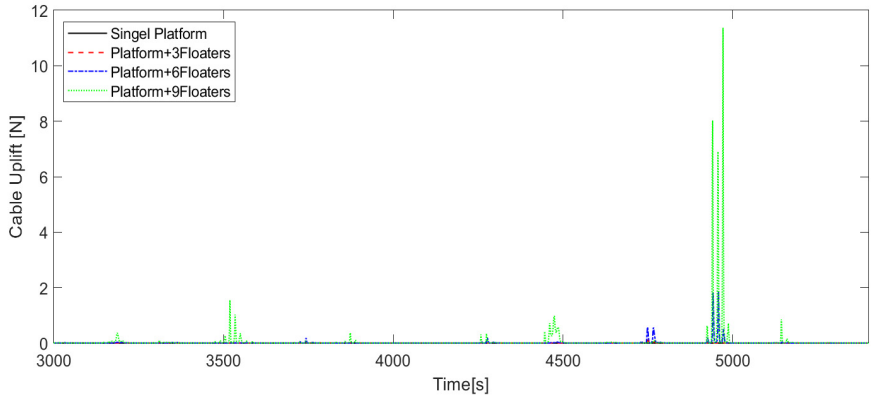


Figure 25. Comparison of anchor force of cable 2 under different models.

After comparing the mooring response, the mooring line strength was evaluated to ensure it meets regulatory standards and prevents breakage. Using R3 grade chains according to DNV standards [33], the breaking strength was calculated to be 1.3829×10^7 N. As shown in Table 7, the maximum mooring force for each model was analyzed, and all safety factors exceeded the minimum requirement of 1.67. This confirms that the mooring

system ensures the safety of the wind-wave power-generation platform with multiple floats under extreme sea conditions.

Table 7. The maximum cable force and its safety factor for each model.

Model	Maximum Cable Force	Safety Factor	Safe or Not
Single Platform	2.4184×10^6	5.72	Safe
Platform + 3floaters	3.0951×10^6	4.47	Safe
Platform + 6floaters	3.6164×10^6	3.82	Safe
Platform + 9floaters	4.3573×10^6	3.17	Safe

5. Conclusions

The validation of the fully coupled analysis confirms the accuracy of F2A coupling between OPENFAST and ANSYS-AQWA.

Simulations under different turbulent wind speeds indicate that the motion response of the floating platform does not vary linearly; it reaches its maximum at the rated wind speed. Similarly, the total power generation of the wave energy converter and the mooring dynamic response follow this pattern. For different oscillating float arrays, changes in the number of floats generally do not affect the mean motion in each degree of freedom of the platform but may slightly increase the peak heave motion and reduce the amplitude of pitch motion.

After introducing wind loads, the average power generation per floater in the array does not increase with the number of floaters; only specific floater arrays can fully utilize each oscillating floater's energy capture capability. The analysis of the combined power-generation platform's motion under different peak spectral periods shows that the motion offset of the floating platform is mainly influenced by the upper wind load, while the peak spectral period primarily affects its amplitude.

The dynamic response results of the wind-wave combined platform under three operational conditions and one survival condition indicate that, compared to wave period, the power generation of the wave energy converter in the lower section is more significantly influenced by wave height. Overall, the combined power-generation platform exhibits the best performance under the third operational condition.

Introducing oscillating floaters under survival conditions can improve the motion response of the floating platform in sway, roll, pitch, and yaw directions to some extent, but it will increase the surge, the heave motion response, and the related mooring loads. After checking the cable strength, it is shown that the mooring system used in this study can ensure the mooring safety of the combined power-generation platform under extreme sea conditions.

Author Contributions: Conceptualization, W.J. and C.L.; methodology, M.C. and J.D.; software, W.J., M.C., and C.L.; validation, C.L., M.C., and Y.Y.; formal analysis, T.T.; investigation, Y.Y. and S.L.; resources, S.L. and W.J.; data curation, C.L.; writing—original draft preparation, C.L.; writing—review and editing, S.L., T.T., and J.D.; visualization, C.L.; supervision, M.C. and W.J.; project administration, Y.Y., S.L., and T.T.; funding acquisition, S.L., Y.Y., and T.T. All authors have read and agreed to the published version of the manuscript.

Funding: This research was funded by Key technology research and demonstration project of 10 MW deep-sea floating offshore wind turbine (DTGD-2023-10174)—Key technology research task of floating offshore combined wind and wave power generation. And this research was also funded by the National Natural Science Foundation of China, grant numbers 5217127. The financial support is greatly appreciated.

Institutional Review Board Statement: Not applicable.

Informed Consent Statement: Not applicable.

Data Availability Statement: Data is contained within the article.

Conflicts of Interest: Author Wei Jiang was employed by the company China Datang Corporation, Ltd. Authors Yi Yang, Tao Tao, and Shi Liu were employed by the company China Southern Power Grid Technology Co., Ltd. The remaining authors declare that the research was conducted in the absence of any commercial or financial relationships that could be considered as a potential conflict of interest.

References

1. Rebecca Williams, F.Z. *Global Offshore Wind Report 2023*; Global Wind Energy Council: Brussels, Belgium, 2023.
2. Bachynski, E.E.; Moan, T. Point Absorber Design for a Combined Wind and Wave Energy Converter on a Tension-Leg Support Structure. In Proceedings of the ASME 2013 32nd International Conference on Ocean, Offshore and Arctic Engineering, Nantes, France, 9–14 June 2013.
3. Yang, Y.; Bashir, M.; Michailides, C.; Li, C.; Wang, J. Development and application of an aero-hydro-servo-elastic coupling framework for analysis of floating offshore wind turbines. *Renew. Energy* **2020**, *161*, 606–625. [CrossRef]
4. Yang, Y.; Bashir, M.; Wang, J.; Yu, J.; Li, C. Performance evaluation of an integrated floating energy system based on coupled analysis. *Energy Convers. Manag.* **2020**, *223*, 113308. [CrossRef]
5. Soulard, T.; Babarit, A.; Borgarino, B.; Wyns, M.; Harismendy, M. C-HyP: A Combined Wind and Wave Energy Platform With Balanced Contributions. In Proceedings of the ASME 2013 32nd International Conference on Ocean, Offshore and Arctic Engineering, Nantes, France, 9–14 June 2013.
6. Zhou, Y.; Ning, D.; Shi, W.; Johanning, L.; Liang, D. Hydrodynamic investigation on an OWC wave energy converter integrated into an offshore wind turbine monopile. *Coast. Eng.* **2020**, *162*, 103731. [CrossRef]
7. Cong, P.; Teng, B.; Bai, W.; Ning, D.; Liu, Y. Wave power absorption by an oscillating water column (OWC) device of annular cross-section in a combined wind-wave energy system. *Appl. Ocean. Res.* **2021**, *107*, 102499. [CrossRef]
8. Jang, H.-K.; Park, S.; Kim, M.-H.; Kim, K.-H.; Hong, K. Effects of heave plates on the global performance of a multi-unit floating offshore wind turbine. *Renew. Energy* **2019**, *134*, 526–537. [CrossRef]
9. Li, J.; Shi, W.; Zhang, L.; Michailides, C.; Li, X. Wind–Wave Coupling Effect on the Dynamic Response of a Combined Wind–Wave Energy Converter. *J. Mar. Sci. Eng.* **2021**, *9*, 1101. [CrossRef]
10. Cheng, Z.; Wen, T.R.; Ong, M.C.; Wang, K. Power performance and dynamic responses of a combined floating vertical axis wind turbine and wave energy converter concept. *Energy* **2019**, *171*, 190–204. [CrossRef]
11. Peiffer, A.; Roddier, D.; Aubault, A. Design of a Point Absorber Inside the WindFloat Structure. In Proceedings of the ASME 2011 30th International Conference on Ocean, Offshore and Arctic Engineering, Rotterdam, The Netherlands, 19–24 June 2011; pp. 247–255.
12. Ren, N.; Ma, Z.; Fan, T.; Zhai, G.; Ou, J. Experimental and numerical study of hydrodynamic responses of a new combined monopile wind turbine and a heave-type wave energy converter under typical operational conditions. *Ocean. Eng.* **2018**, *159*, 1–8. [CrossRef]
13. Li, L.; Yuan, Z.-M.; Gao, Y.; Zhang, X.; Tezdogan, T. Investigation on long-term extreme response of an integrated offshore renewable energy device with a modified environmental contour method. *Renew. Energy* **2019**, *132*, 33–42. [CrossRef]
14. Si, Y.; Chen, Z.; Zeng, W.; Sun, J.; Zhang, D.; Ma, X.; Qian, P. The influence of power-take-off control on the dynamic response and power output of combined semi-submersible floating wind turbine and point-absorber wave energy converters. *Ocean Eng.* **2021**, *227*, 108835. [CrossRef]
15. Wang, B.; Deng, Z.; Zhang, B. Simulation of a novel wind–wave hybrid power generation system with hydraulic transmission. *Energy* **2022**, *238*, 121833. [CrossRef]
16. Wang, Y.; Huang, S.; Xue, G.; Liu, Y. Influence of Hydraulic PTO Parameters on Power Capture and Motion Response of a Floating Wind-Wave Hybrid System. *J. Mar. Sci. Eng.* **2022**, *10*, 1660. [CrossRef]
17. Chen, M.; Jiang, J.; Zhang, W.; Li, C.B.; Zhou, H.; Jiang, Y.; Sun, X. Study on Mooring Design of 15 MW Floating Wind Turbines in South China Sea. *J. Mar. Sci. Eng.* **2024**, *12*, 33. [CrossRef]
18. Liu, H.; Chen, M.; Han, Z.; Zhou, H.; Li, L. Feasibility Study of a Novel Open Ocean Aquaculture Ship Integrating with a Wind Turbine and an Internal Turret Mooring System. *J. Mar. Sci. Eng.* **2022**, *10*, 1729. [CrossRef]
19. CCS. *Design and Evaluation of Offshore Structures Environmental Conditions Application Guide 2021*; CCS: Beijing, China, 2021; Volume GD04-2021.
20. Zou, M.Y.; Chen, M.S.; Zhu, L.; Yun, Q.H.; Zhao, W.H.; Liang, Q.Y.; Zhao, Y.J. Experimental and numerical investigation of gap resonances between side-by-side fixed barges under beam sea excitation. *Ocean Eng.* **2024**, *297*, 117150. [CrossRef]
21. Chen, M.; Deng, J.; Yang, Y.; Zhou, H.; Tao, T.; Liu, S.; Sun, L.; Hua, L. Performance Analysis of a Floating Wind–Wave Power Generation Platform Based on the Frequency Domain Model. *J. Mar. Sci. Eng.* **2024**, *12*, 206. [CrossRef]
22. Chen, M.; Ouyang, M.; Guo, H.; Zou, M.; Zhang, C. A Coupled Hydrodynamic-Structural Model for Flexible Interconnected Multiple Floating Bodies. *J. Mar. Sci. Eng.* **2023**, *11*, 813. [CrossRef]
23. Chen, M.; Xiao, P.; Zhang, Z.; Sun, L.; Li, F. Effects of the end-stop mechanism on the nonlinear dynamics and power generation of a point absorber in regular waves. *Ocean Eng.* **2021**, *242*, 110123. [CrossRef]
24. Zou, M.; Chen, M.; Zhu, L.; Li, L.; Zhao, W. A constant parameter time domain model for dynamic modelling of multi-body system with strong hydrodynamic interactions. *Ocean Eng.* **2023**, *268*, 113376. [CrossRef]

25. Li, Y.; Ong, M.C.; Wang, K.; Li, L.; Cheng, Z. Power performance and dynamic responses of an integrated system with a semi-submersible wind turbine and four torus-shaped wave energy converters. *Ocean Eng.* **2022**, *259*, 111810. [CrossRef]
26. Tian, W.; Wang, Y.; Shi, W.; Michailides, C.; Wan, L.; Chen, M. Numerical study of hydrodynamic responses for a combined concept of semisubmersible wind turbine and different layouts of a wave energy converter. *Ocean Eng.* **2023**, *272*, 113824. [CrossRef]
27. Chen, M.; Wang, R.; Xiao, P.; Zhu, L.; Li, F.; Sun, L. Numerical Analysis of a Floating Semi-Submersible Wind Turbine Integrated With a Point Absorber Wave Energy Convertor. In Proceedings of the 30th International Ocean and Polar Engineering Conference, Shanghai, China, 11–16 October 2020.
28. Yu, W. *Qualification of Innovative Floating Substructures for 10MW Wind Turbines and Water Depths Greater than 50m*; University of Stuttgart: Stuttgart, Germany, 2018.
29. Kamarlouei, M.; Gaspar, J.F.; Calvario, M.; Hallak, T.S.; Mendes, M.J.G.C.; Thiebaut, F.; Guedes Soares, C. Experimental study of wave energy converter arrays adapted to a semi-submersible wind platform. *Renew. Energy* **2022**, *188*, 145–163. [CrossRef]
30. Bak, C. *DTU Wind Energy Report-I-0092*; DTU Wind Energy: Roskilde, Denmark, 2013.
31. Hu, J.; Zhou, B.; Vogel, C.; Liu, P.; Willden, R.; Sun, K.; Zang, J.; Geng, J.; Jin, P.; Cui, L.; et al. Optimal design and performance analysis of a hybrid system combing a floating wind platform and wave energy converters. *Appl. Energy* **2020**, *269*, 114998. [CrossRef]
32. Chen, M.; Yuan, G.; Li, C.B.; Zhang, X.; Li, L. Dynamic Analysis and Extreme Response Evaluation of Lifting Operation of the Offshore Wind Turbine Jacket Foundation Using a Floating Crane Vessel. *J. Mar. Sci. Eng.* **2022**, *10*, 2023. [CrossRef]
33. Barrera, C.; Battistella, T.; Guanche, R.; Losada, I.J. Mooring system fatigue analysis of a floating offshore wind turbine. *Ocean Eng.* **2020**, *195*, 106670. [CrossRef]

Disclaimer/Publisher's Note: The statements, opinions and data contained in all publications are solely those of the individual author(s) and contributor(s) and not of MDPI and/or the editor(s). MDPI and/or the editor(s) disclaim responsibility for any injury to people or property resulting from any ideas, methods, instructions or products referred to in the content.